HEAT TRANSFER ENHANCEMENT OF A PERMANENT MAGNET SYNCHRONOUS MACHINE

IN VEHICLE TRACTION

(PUBLIC VERSION)

VINAY BHARADWAJ SRISANKAR

DC SYSTEMS ENERGY CONVERSION AND STORAGE,
FACULTY OF ELECTRICAL ENGINEERING, MATHEMATICS AND
COMPUTER SCIENCE

Delft
University of
Technology

HEAT TRANSFER ENHANCEMENT OF A PERMANENT MAGNET SYNCHRONOUS MACHINE USED IN VEHICLE TRACTION

(PUBLIC VERSION)

by

Vinay Bharadwaj Srisankar

to obtain the degree of Master of Science at the Delft University of Technology, to be defended publicly on Tuesday July 10, 2015.

Student number:	4304799	
Project duration:	Nov, 2014 – July, 2015	
Thesis committee:	Dr. ir. Henk Polinder,	TU Delft, supervisor
	Dr. D. J. P. Lahaye,	TU Delft
	Dr. ir. M. J. B. M. Pourquie,	TU Delft
	Ir. Yang Tang,	e-Traction Europe B.V.

Delft
University of
Technology

ABSTRACT

One of the major restrictions that hinder the versatility of electrical machines in any sector is their thermal limitations. This thesis deals with the study of the heat transfer occurring in an outer rotor permanent magnet synchronous machine used in the electric vehicle industry with the aim of exploring possibilities to reduce the hotspot temperature. The project is in collaboration with e-Traction, an electric vehicle systems designer. A 3D numerical model of the machine is designed using the Finite Element Method (FEM) with heat transfer coefficients obtained from a computational fluid dynamics (CFD) simulation. A closer look at the secondary flow with vortices in curved tubes is also presented as part of the pursuit to estimate boundary conditions required for the FEM model. The equivalent thermal conductivity of the slot region was estimated by a 2D FEM model and the external heat transfer coefficients were represented using empirical relations. The model was validated with experimental tests performed at the e-Traction's test bench facility and was found to be sufficiently accurate to predict the influence of material and mechanical design changes on the heat transfer. Results show that by using certain potting materials and making slight changes in the cooling region, hotspot temperatures can be significantly reduced.

ACKNOWLEDGMENTS

This thesis was initiated as a joint project between the Delft University of Technology and e-Traction. The subject of this thesis spanned multiple disciplines and gave me the opportunity to explore most of them. I would like to extend my gratitude towards Henk Polinder for giving me the opportunity to be part of this collaboration and to instil the confidence in me to set foot into other subject territories. Martin van der Geest, my daily supervisor guided me through the unknown paths of a new field and was always present to answer technical and non-technical queries (has a great sense of humour!).

I would like to thank Domenico Lahaye from the department of mathematics who first introduced me to the finite element approach and was present throughout my thesis as an additional supervisor. I was also very lucky to attend a course on computational fluid dynamics taught by Mathieu Pourquie who set me on the correct path towards understanding the wonderful world of fluid flow and its simulation.

I thank Peter Paul van der Ven from e-Traction who took the responsibility of being supervisor from the company's side and offered an abundance of help during the thesis. Timothy van Seventer and Yang Tang from e-Traction were also very helpful in arranging test equipment and providing valuable data. During the journey of my thesis, I met many people from different disciplines who all contributed directly or indirectly. I owe a lot to my colleagues from the student rooms who inspired me to work harder. I would also like thank the coffee machines that made working late and on weekends possible.

Last but not least, I would not be where I stand today without the help of my parents. There are no words sufficient enough to thank them.

Vinay Bharadwaj Srisankar
Delft University of Technology

CONTENTS

LIST OF FIGURES

LIST OF TABLES

1

INTRODUCTION

Electric Vehicles (EVs) which offer high performance at reduced fuel costs and emissions are gaining more and more interest in today's environmentally concerned world. Here combustion engines are replaced by efficient electric motors and fuel tanks by battery packs which have the capability to recharge as the vehicle coasts. There has been a lot of interest in comparing electric machines for traction applications ([1]) of which the Permanent Magnet Synchronous Machine is gaining prominence for their advantages over other types([2]). Electrical motors despite offering high efficiency, are restricted by electromagnetic and thermal factors which are in some ways interconnected.

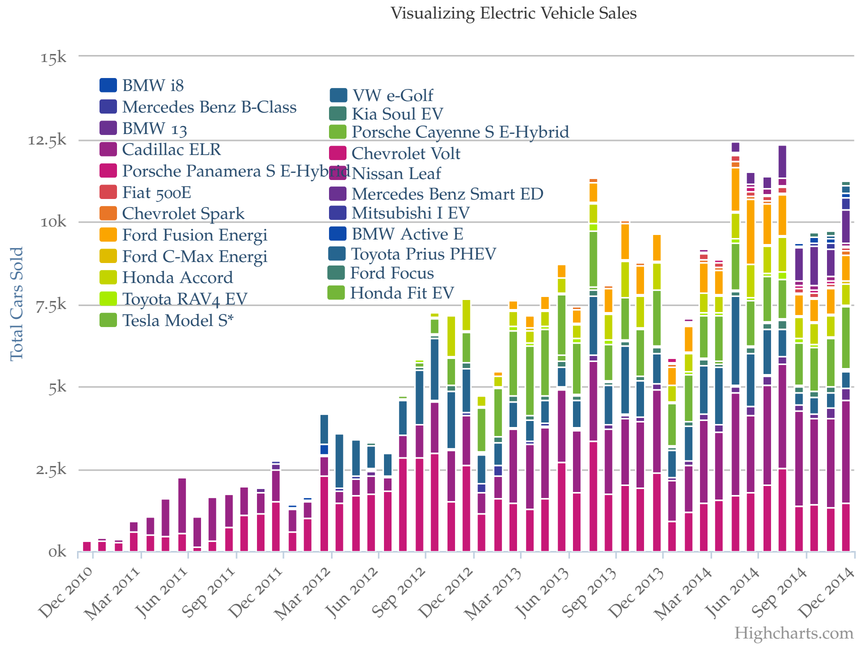

Figure 1: Electric Vehicle Car sales on the rise
www.energy.gov

E-Traction, a pioneer in the field of e-mobility manufactures Permanent Magnet Synchronous Machines (PMSM) which are used as **in-wheel motors** for electric buses. The *HUB* motors offer several advantages ([3, 4]) like eliminating the electrical and electronic space requirements on-board the chassis to providing more passenger and battery space. Since they are directly connected to the rim of the wheel, the losses associated with transmission are also reduced leading to an increased over-all efficiency. There are however a few disadvantages like wheel mass to body mass ratio which reduces the affinity to such designs, but this does not play a significant role in some applications ([5]).

Permanent Magnet Machines offer high power densities due to the compactness of magnets but in the transportation sector machines need to adhere to strict standards such as water proofing, dust protection etc. restricting the possibility of using air as a method of heat removal. As a consequence of this, designers resort to other methods such as (in our case) cooling channels in the inner periphery of the machine to keep it from becoming too hot. There are also various levels of insulation provided between the winding and the cooling channels made of poor thermal materials that inhibit the cooling system from performing well.

1.1 PROBLEM DESCRIPTION

The power density of the PMSM like any other electrical machine is restricted by the thermal limits of its insulation. The windings are of class F insulation which has a maximum rated temperature of 155 degC meaning that it has to be maintained under this temperature for a good life (approximately 20,000 hours). An increase in 10degC halves the lifetime of the machine and so any improvement in temperature has a direct impact on the life of the machine. The resistance of the copper windings also increase with temperature, so lower temperatures result in a lower loss which runs iteratively. Having all these in mind, a method to predict the hotspot temperatures under any operating condition and to be able to explore methods to keep them satisfactorily low, is highly beneficial to allow for higher currents to be used. Implementing design changes or trying out new improved materials is rather not practical on a real machine due to cost and time limits, thus people resort to digital models of the machine which behave in a similar way. This thesis aims at deriving a model and observing the changes in thermal behaviour within that model under different conditions and designs.

An analytical model comprises of equations describing characteristics of the system under prescribed operating variables. They are fast and require very little computational time, but rely heavily upon correlations to obtain certain parameters. Despite the fact that there is a large database of empirical relations today, they are restricted by the type of machine, dimensions and shapes of the cooling regions. An example of an analytical method is the *Lumped Parameter Network* which uses the principles of electrical circuits to estimate temperatures in certain regions.

Temperature Tolerance Class	Maximum Operating Temperature Allowed
A	105 °C
B	130 °C
F	155 °C
H	180 °C

Table 1: Insulation limits from NEMA
www.engineeringtoolbox.com

A numerical model on the other hand deals with taking the geometry and splitting it into small regions of computation capable of producing a three dimensional graphical overview of the results. They are computationally demanding but are accurate, do not depend as much on correlations and with today's hardware capabilities are more and more user friendly. There has been a long standing discussion about which technique to utilize and there have been several studies that compare both [6] giving mixed results.

The thermal modelling by any technique is however not straightforward. The machines temperature is also dependent on the electromagnetic losses and the influence of the fluid dynamics. Some studies make use of thermal lumped networks by making assumptions for the electromagnetic and fluid parameters([7]) while some ([8]) do an in depth analysis by coupling the electromagnetic and thermal physics into a single model and utilizing empirical relations for the fluid dynamics. The latter provides a better understanding of the processes occurring inside the machine. The use of assumptions is made possible due to the availability of experimentally verified correlations in literature ([9],[10]). With the help of such studies, many unknown parameters can be approximated but may not be valid for all conditions and designs. Hence some authors have resorted to performing their own computational fluid dynamics simulations and estimating boundary conditions for a coupled electromagnetic and thermal simulation([11]). Thermal models not only provide a plethora of insight but also make possibilities for electrical improvements and mechanical design optimizations ([12],[13],[14]).

1.2 SCOPE OF THIS THESIS

Modelling techniques are ultimately just tools that can be used to analyse a collection of data. The identification of the right data corresponding to the machine is still common to both techniques. This thesis makes use of two numerical schemes the *Finite Volume Method* and the *Finite element Analysis* to help realize the ultimate goal of analysing the machine temperature distribution. To obtain design specific convection parameters, a computational fluid dynamics simulation is run and results are applied to an electric current - heat transfer model. The losses are estimated by an electro-magnetic simulation. The final integrated model is utilized to evaluate design and material suggestions.

1.2.1 *Structure of the thesis*

The data we require for the computation can be split into two parts, conductivity parameters which describe heat transfer between and within solids, and convection parameters that describe the influence of a moving fluid on heat transfer. **Chapter 2** introduces the basic design of the machine and reviews various studies performed to estimate of the thermal conductivities in detail. **Chapter 3** is structured similarly but with focus on the estimation of convection coefficients. It will be seen that one of the critical convection coefficients requires a more in-depth analysis and thus a numerical simulation was performed whose results are briefly discussed. **Chapter 4** describes the integration of the data collected from chapters 2 and 3 to perform a final heat transfer simulation. **Chapter 5** suggests methods to reduce the machine temperature by varying the influential parameters identified in Chapter 3 and by analysing changes in materials. Finally **Chapter 6** concludes the research conducted and suggests improvements for future studies.

2

MODEL PREREQUISITES - MACHINE DESIGN AND MATERIAL PROPERTIES

This chapter explains the structure of the current machine and the estimation of the various thermal resistances and conduction parameters that have to be incorporated into the numerical model later. The chapter also introduces the various sources of heat that are generated in the machine which have been obtained from a collaborative research

2.1 CURRENT MACHINE

The PMSM under study has of an outer rotor with surface mounted magnets whose specifications are shown in the glossary. The exploded view of the machine is shown in the Fig 2 where we see several layers of materials that have to be described separately to ensure a clear understanding.

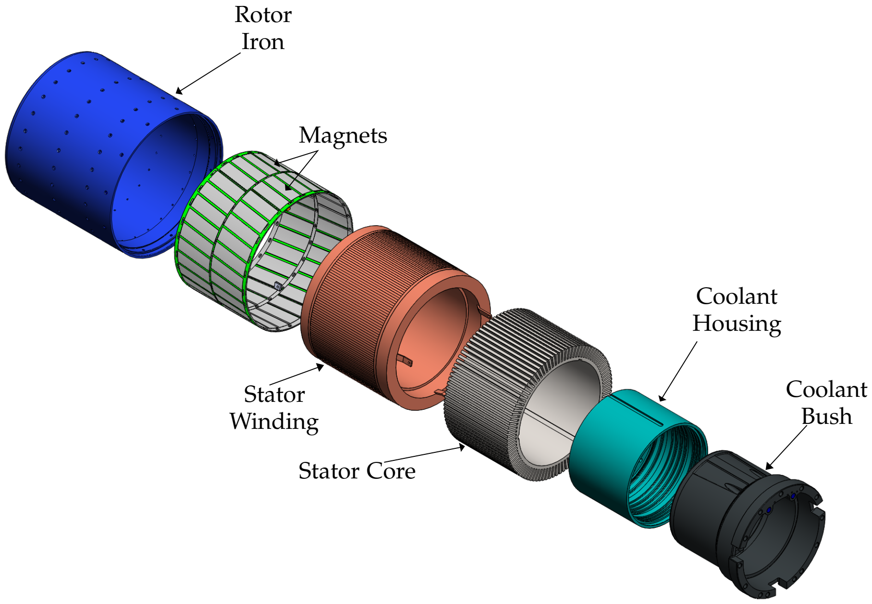

Figure 2: The exploded view of the current machine

2.1.1 *Stator Core and Windings*

The Stator core is made up of a number of thin laminations which have been assembled to form the shape of the core. There are N_{slot} slots where the windings are placed and are notched on the tips as shown in Fig. 3. There are N_{phase} per slot and N_{turn} per phase. There is a slot wedge above the windings to keep them intact during operation. Due to the possibility of wear and tear between the windings and the stator, there are slot liners present which play a dual role of smoothing and electrical isolation.

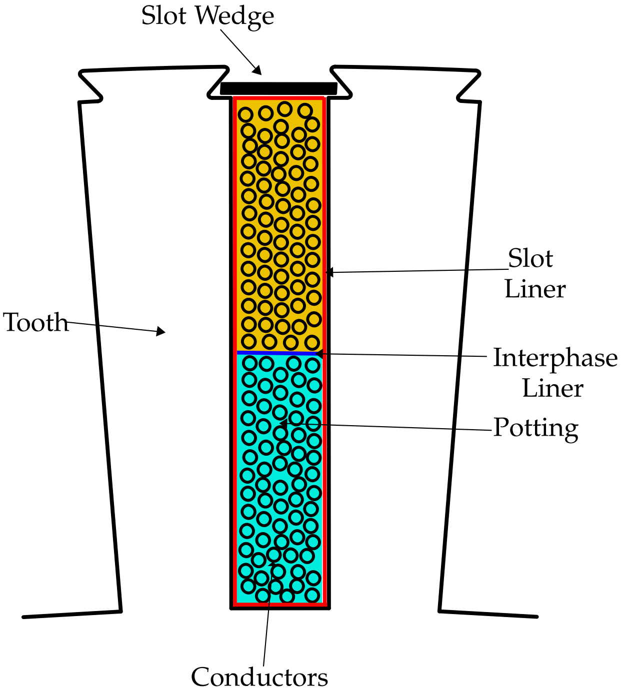

Figure 3: A section of the stator core with the windings

A single phase winding is comprised of N_{strand} copper strands of D_{cu} diameter that are bunched together to carry more current. There are three such phases which are arranged around the core in a **distributed winding pattern**. After arrangement, the slot is filled with what is called the potting compound to ensure that the windings do not rub against each other with vibration and to enhance heat transfer between them and the stator. The Stator core is l_{ax} long and at either end, the windings extend outside of the slot to reach their consecutive position (N_{pitch} poles long). This region is called the end winding and is shown in Fig.4.

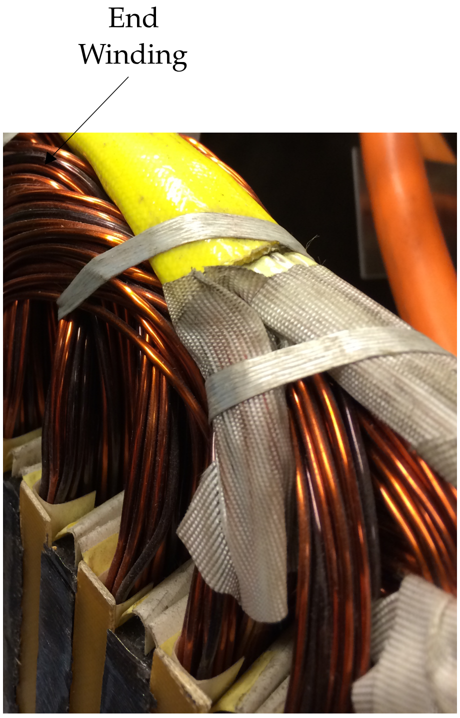

Figure 4: The end winding of the machine

2.1.2 *Rotor and Magnets*

There are N_{magnet} magnets arranged around the inner periphery of the rotor in two columns axially. The two rows are displaced from each other and the magnets themselves are inclined to the axis of the rotor as shown in Fig. 5, this is called *skewing* of the magnets and is done to reduce the cogging of the rotor (vibrations in rotation due to magnet stator attraction). The magnets are held in their places using a strong adhesive and a pattern holder. The air-gap between the stator and rotor is l_g in length from the inner face of the magnet to the outer face of the pole.

2.1.3 *The cooling region*

The cooling channels are carved out of the inner periphery of the housing where there are nine channels of different dimensions which are linked to a common flow distribution space. The fluid space is basically created when the housing and the stator carrier are fit air-tight together. In Fig. 6 the section view of the housing reveals the arrangement of the channels. The coolant used in this machine is 50% diluted Ethylene Glycol an industrial anti-freeze used for operation under sub-zero conditions.

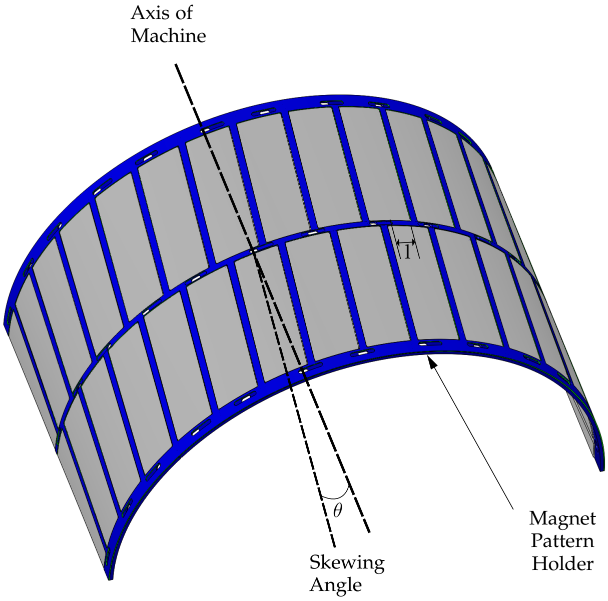

Figure 5: Magnet Skewing and Displacement

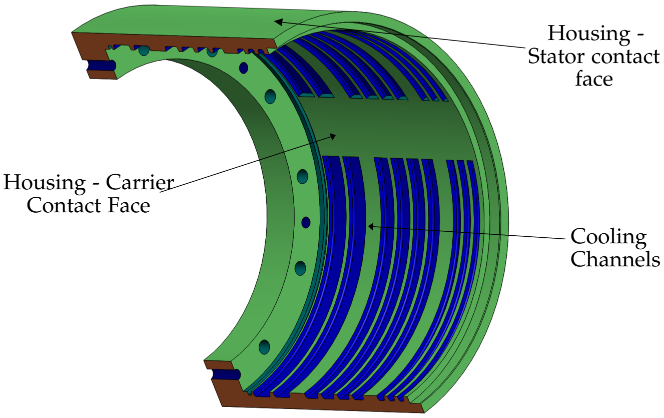

Figure 6: Section of the Aluminium coolant housing

2.2 PARAMETER ESTIMATION

A model is only as good as the properties and boundary conditions specified to it. There are different approaches to the estimation of these,the first is adopted by Guemo et al. who uses algorithms to calculate parameters that can be directly applied to analytical models. The second approach is to rely on a database of experimental results for certain uncomputable parameters and deduce the rest through simulations.

2.2.1 *Material Properties*

When ever there exists a Temperature gradient in a stationary medium, there will be a heat transfer that will follow, this is termed as *conduction*. The higher temperature region contains molecules of higher energy than in the lower and upon collision, there will be an exchange of energy. This is the fundamental physics that constitute conduction and it can be quantified with a property called *Thermal Conductivity* represented by λ. It is a material specific property and the table below shows the thermal conductivities of the materials in the machine.

Material	Thermal Conductivity (k) (W/mK) 25 °C	Heat Capacity at Constant Pressure (Cp) (J/kgK)
Stator Iron - Radial	36	420
Winding Copper	380	385
Winding Insulation	0.15	1000
Potting Compound	0.71	1800
Slot Liner	0.156	260
Coolant Housing (Al)	167	900
Air (Dry)	0.0267	1005
Magnets axial/radial	$\lambda_{mag-ax}/\lambda_{mag-r}$	C_{p-mag}
Rotor Back Iron	21.8	461
Rim	44.5	475

Table 2: Various material properties from data-sheet and manufacturer

These properties are readily available from databases/manufacturers. There are however other thermal barriers within the machine that have to be calculated or estimated by experiments.

2.2.2 *Equivalent Thermal Conductivity of the Slot*

The winding region of the machine as seen earlier is composed of a composite of different materials each having a part to play in the overall thermal conductivity. It is rather cumbersome and computationally expensive to be able to model the entire winding in detail and thus a simple geometry with effective properties are required. This has been the focus of many researchers in the past who used different representations to deduce the equivalent thermal conductivity of this region. The work of Simpson et al. mentions an analytical approximation given by Hashin and Shtrikman based on volume ratios of the winding constituents that can be applied for cylindrical conductors.This methods was experimentally validated and shows a good correlation with reality. If we consider $v_c, v_{ii} and v_{ci}$ as the volume ratios of the conductor, impregnation insulation and winding insulation respectively; we can write:

$$v_c + v_{ci} = PF \tag{1}$$

$$v_c + v_{ii} + vci = 1 \tag{2}$$

$$v_c = PF(\frac{r_c^2}{(r_c + l_i)^2}) \tag{3}$$

$$v_{ci} = PF(\frac{(2r_c l_i) + l_i^2}{(r_c + l_i)^2} \tag{4}$$

$$k_e = k_a \frac{(1 + v_c)k_c + (1 - v_c)k_a}{(1 - v_c)k_c + (1 + v_c)k_a} \tag{5}$$

Here PF is the packing factor that gives the ratio of the area of winding (Winding and its insulation) to the area of the slot. k_a is the equivalent thermal conductivity of the winding insulation and impregnation calculated based on their volumetric contributions based on equation 6.

$$k_a = k_{ii} \frac{v_{ii}}{v_{ii} + v_{ci}} + k_{ci} \frac{v_{ci}}{v_{ii} + v_{ci}} \tag{6}$$

Another approach to calculate the equivalent thermal conductivity would be through a 2D Finite Element Approach represented by Fig.7. A heat source Q is specified on top end of the slot and a temperature condition is applied to the bottom. With all the material geometries and properties specified, we can calculate the equivalent thermal conductivity based on the equation 7:

$$k = \frac{P_w l_1}{(T_1 - T_2)A} \tag{7}$$

Here the P_w is the power in watts introduced into the slot and A, the area normal to the heat plate.

The final value of *effective thermal conductivity* that can be used in the model is however still dependent on one other factor, the *impregnation goodness*. This factor is basically the ratio of air bubbles to the potting which are introduced during the impregnation process. Methods like Vacuum Pressure Impregnation (VPI) can introduce as low as 25% air with low viscosity potting material (Nategh et al.,Boglietti et al.). The method used on the current machine is gravity driven that allows the potting compound to fill the spaces under the influence of its own weight. This method is not a recommended method and we assume

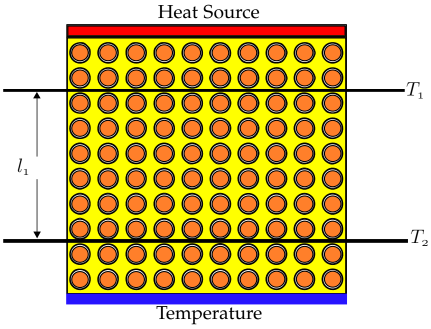

Figure 7: 2D Finite Element Model representation of Winding composite

a goodness factor of 60% (40% air) which is represented by 0.4 times the thermal conductivity of air plus 0.6 times that of the winding.

From the thermal conductivities shown in table 3, it can be inferred that the analytical approximation has a slightly higher value compared to FEM. From literature we learn that the FEM model is more accurate, thus it is used further.

Method	k (W/mK)
H+S Approximation	1.3946
FEM Model	1.102

Table 3: Thermal conductivities calculated by both methods

2.2.3 *Inter-facial Gaps*

Two solids in contact contain irregularities that tend to introduce air gaps providing a higher thermal resistance. The heat transfer through a gap may be considered to be made of the following components (Salerno and Kittel):

- Conduction through actual contact spots
- Conduction through the interstitial medium such as gas.
- Radiation

The inter-facial gaps are too small for bouyancy effects to set up and under temperatures of 300 °C radiation effects can also be neglected leaving us with only conduction. There will be a temperature drop across this interface as a result of which an additional heat flux will exist. This additional resistance can be represented by a thermal contact conductance, h is given be eqn 8.

$$h = \frac{Q/A}{\Delta T} \tag{8}$$

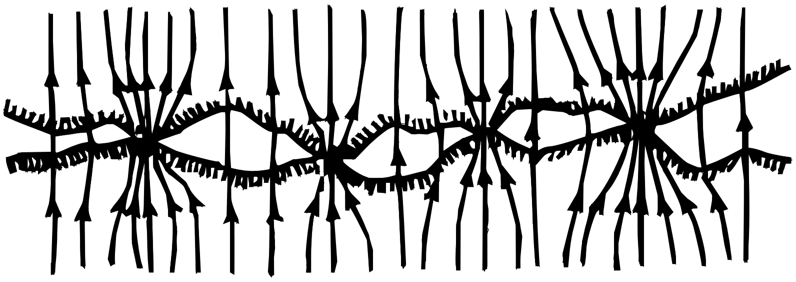

Figure 8: A magnified view of an interface contact
source: *thermopedia.com*

Q is the total heat flow and A is the nominal contact area. The value of contact conductance can be represented by an equivalent air gap to represent the thermal resistance along this path.

In this machine, there are primarily two interfaces that play a vital role in heat transfer.

- The interface between the Stator core and the Aluminium coolant housing
- The Interface between the slot liner and the stator core.

The fluid housing is fit with the stator core though a process called interference fitting. Here the former is cooled to cause a shrinkage of volume for positioning and then is allowed to return to its original volume at room temperature. This causes a contact pressure at the surface and thus a corresponding contact conductance. Studies have shown that the equivalent air gap reduces with increase in contact pressure and smoothness of the two interfaces (Kulkarni et al.). The exact value of this equivalent gap is hard to predict and must be either experimentally determined or taken from literature like Boglietti et al. which states various gap lengths for induction machines of different ratings. Material specific data is also extremely useful to help estimate this value in any electrical machine like table 4 taken from works of Staton et al..

These values cannot be considered constant for this situation as they are highly dependent on the temperature conditions at the interface. Higher temperatures (caused by higher heat flux) cause thermal expansion (Camilleri et al.) which either loosen or tighten the gap (based on the material at the inner periphery).

The machine studied here has the coolant housing made from aluminium at the inner periphery of the stator laminations, and based on the difference in thermal expansion rates given in table 5 the housing should press against the stator with temperature leading to the assumption that as the machine heats up this interface gap reduces.

Materials	Interface Conductance (W/m^2K)	Effective Gap (mm)
Ceramic-Ceramic	500-3000	0.0087-0.0052
Ceramic-Metal	1500-8500	0.0031-0.0173
Graphite -Metal	3000-6000	0.0043-0.0087
Stainless-Stainless	1700-3700	0.0070-0.0153
Aluminium-Aluminium	2200-12000	0.0022-0.0012
Stainless-Aluminium	3000-4500	0.0058-0.0087
Iron-Aluminium	4000-40000	0.0006-0.0060
Copper-Copper	10000-25000	0.0010-0.0026

Table 4: Material specific interface conductances

Material	Thermal Expansion Coefficient ($10^{-6}m/m-K$)
Aluminium	22.6
Stator Core	11.9
Copper	16.6

Table 5: Coefficient of thermal expansion of materials

We thus create a function that asymptotes to a fixed gap length with temperature based on steady state experimental results, this will be looked into in detail in the next chapter.

The slot liner is placed into the stator slot before the impregnation process and this tends to introduce small air gaps under it. There have been very few studies that look into this, partially because of its dependence on the type, size and application of the machine. Kylander mentions certain lengths of this gap which can serve as a good first approximation(0.17mm for a 4kW machine and 0.30mm for a 15kW machine). There is also thermal expansion here that may prevent the use of a single value.

2.3 HEAT SOURCES

The electric machine heats up due to the various losses dissipated. These are classified based on their origin as:

- Copper Losses
- Iron/Core Losses
- Mechanical losses

The first two losses are explained in detail in this section.

2.3.1 *Copper Losses*

The copper loss originates from Joule's Law of heating which states that the amount of heat in watts dissipated by the conductor is proportional to its resistance and the square of the current flowing through it, mathematically depicted in eqn 9:

$$P_{Cu} = mI^2 R_{AC} \tag{9}$$

m denotes the number of phases,I, the current and R_{AC} is the A.C. resistance of the machine which takes into account the additional resistance due to skin effect (not present in this machine due to low operating frequencies). This varies linearly as a function of temperature based on eqn 10:

$$R(T) = R(T_o)(1 + \alpha \Delta T) \tag{10}$$

where T_o is the room temperature and α is known at the *Temperature Coefficient of Resistance*. For Copper $\alpha = 3.86 * 10^{-3}/°\mathrm{C}$.

2.3.2 *Iron/Core Losses*

The machine is exposed to alternative fluxes in many regions due to time varying currents and the relative motion of the magnets. These tend to induce voltages in the ferromagnetic regions of the machine that establish circulating currents which try to resist this change in flux. These are called eddy currents and dissipate heat on account of the material resistivity. To reduce these losses, the stator is composed of thin laminations stacked together disconnecting the path longitudinally for the eddy currents, but there will still be currents circulating in the plane of the lamination. The power losses associated with the eddy currents can be expressed as in eqn 11 [22]:

$$P_{Fe} = \frac{V.\pi^2 f^2 d^2 B_{max}^2}{6\rho} \tag{11}$$

where V is the volume of the lamination, *f*, frequency, B_m is magnetic flux density, d is thickness of lamination and ρ is the resistivity of the lamination material.

Another consequence of the varying fluxes is the *hysteresis losses*, caused by the BH loop of the material. Empirical relations yield:

$$P_{Hy} \propto V f B_{max}^n \tag{12}$$

These two losses together constitute the Iron losses. Further information about these losses can be obtained from Pyrhönen et al.

From the mathematical representations above, it can be seen that the iron losses require the calculation of the Magnetic flux density which by itself is not analytically straightforward. Therefore, the data for these losses are taken from a parallel thesis within the same project dealing with the *Design optimization of Surface mounted permanent magnet machines for electric vehicle applications* where an electromagnetic simulation is performed to estimate the flux densities in the machine regions which can then be converted into a loss value from tabulations in the lamination material datasheet.

3

MODEL PREREQUISITES: CONVECTION COEFFICIENTS

This chapter discusses the estimation of all convection coefficients (fluid - solid interaction) required to complete the numerical model. A small introduction to fluid mechanics is presented to aid the understanding of such processes occurring within the machine. One of the convection parameters requires a simulation to be performed using Computational Fluid Dynamics and will be discussed in more detail.

3.1 PROBLEM DESCRIPTION

As heat is generated within the machine there is a simultaneous dissipation to the surrounding air and cooling fluid. The rate at which heat is dissipated depends on the parameter called *Convective heat transfer coefficient* which in turn depends on various other factors like fluid velocity etc. We require the approximate values of these convection coefficients where ever there is gas or liquid in contact with a solid. Fig. 9 shows the cross section of the machine and the regions where fluid and solid interaction takes place.

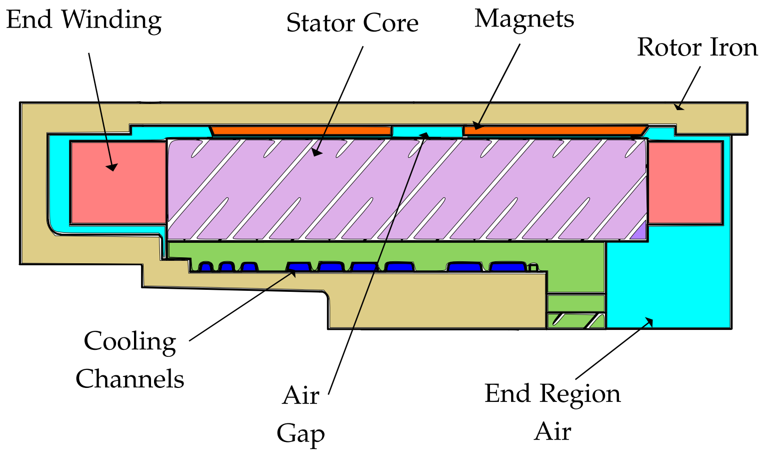

Figure 9: Cross section of the machine revealing the fluid regions

There are four regions where these interfaces are seen, *the end winding region*, *air-gap* , *cooling channels* and the *the outer rotor surface*.

We need to know how the heat transfer occurs at these interfaces before we can quantify and assume values. To aid that, the following sections briefly discuss the fundamentals of fluid dynamics split as follows:

3.2 Governing equations

3.3 Flow over flat plate

3.4 Flow within a pipe

3.5 Pressure drop in pipes

Post which there is a literature study performed to estimate values for the convection coefficients relating to the machine. Further information regarding the fundamentals can be found in Tu et al.. It should be noted that the type of flow decides the behaviour of the fluid and thus their governing equations. This is based on whether it is a *laminar flow* or *turbulent flow* (A transition region also exists between the two). Turbulent flows show random three-dimensional fluid motion whereas laminar flows are more uniform and steady in nature. We shall only look into laminar flows because of its application in our case. For further information on turbulence, one can refer Incropera et al..

3.2 GOVERNING EQUATIONS

One of the fundamental laws describing the fluid flow is conservation of mass which states that matter can neither be created nor be destroyed. It can be expressed as shown in equation 13 where the u,v and w are the local velocities at x,y and z respectively and t is the time.

$$\frac{\partial \rho}{\partial t} + \frac{\partial(\rho u)}{\partial x} + \frac{\partial(\rho v)}{\partial y} + \frac{\partial(\rho w)}{\partial z} = 0 \tag{13}$$

This equation is also known as the continuity equation. If we consider incompressible flow, the equation is further simplified to

$$\frac{\cancelto{0}{\partial \rho}}{\cancel{\partial t}} + \rho(\frac{\partial u}{\partial x} + \frac{\partial v}{\partial y} + \frac{\partial w}{\partial z}) = 0 \tag{14}$$

Another set of equations which are extremely important in fluid dynamics are the momentum equations essentially derived from the continuity equations stated earlier and from Newton's second law of motion (15 to 17).

$$\underbrace{\frac{\partial u}{\partial t}}_{\text{local acceleration}} + \underbrace{u\frac{\partial u}{\partial x} + v\frac{\partial u}{\partial y} + w\frac{\partial u}{\partial z}}_{\text{advection}} = \underbrace{-\frac{1}{\rho}\frac{\partial p}{\partial x}}_{\text{pressure gradient}} + \underbrace{\nu(\nabla^2 u)}_{\text{diffusion}} \tag{15}$$

$$\underbrace{\frac{\partial v}{\partial t}}_{\text{local acceleration}} + \underbrace{u\frac{\partial v}{\partial x} + v\frac{\partial v}{\partial y} + w\frac{\partial w}{\partial z}}_{\text{advection}} = \underbrace{-\frac{1}{\rho}\frac{\partial p}{\partial y}}_{\text{pressure gradient}} + \underbrace{\nu(\nabla^2 v)}_{\text{diffusion}} \tag{16}$$

$$\underbrace{\frac{\partial w}{\partial t}}_{\text{local acceleration}} + \underbrace{u\frac{\partial w}{\partial x} + v\frac{\partial w}{\partial y} + w\frac{\partial w}{\partial z}}_{\text{advection}} = \underbrace{-\frac{1}{\rho}\frac{\partial p}{\partial z}}_{\text{pressure gradient}} + \underbrace{\nu(\nabla^2 w)}_{\text{diffusion}} \tag{17}$$

Here $''\nu''$ is the kinematic viscosity which is a fluid property and $''p''$ is the pressure. These equations describe the local acceleration and dissipation of momentum in the presence of external forces such as pressure and viscous forces.

Lastly, the conservation of energy is explained which is derived from the *first law of thermodynamics* which states that:

$$\begin{array}{c}\text{The change in internal}\\ \text{Energy of a System}\end{array} = \begin{array}{c}\text{Heat added}\\ \text{to the system}\end{array} + \begin{array}{c}\text{Workdone by}\\ \text{the system}\end{array} \tag{18}$$

By incorporating *Fourier's Law of heat conduction* and after simplification, the Energy Equation yields:

$$\underbrace{\frac{\partial T}{\partial t}}_{\text{Local Temperature rise}} + \underbrace{u\frac{\partial T}{\partial x} + v\frac{\partial T}{\partial y} + w\frac{\partial T}{\partial z}}_{\text{advection}} = \underbrace{\frac{\lambda}{\rho C_p}(\nabla^2 T)}_{\text{diffusion}} + S \tag{19}$$

This equation 19 explains that the rise in temperature at a point in time is dependent upon the heat carried by moving fluid (called advection) and the dispersion of heat due to molecular phenomena (called diffusion). λ is the thermal conductivity, C_p is the specific heat capacity at constant pressure of the fluid and S is the source of heat (Iron and/or Copper Losses in our system).

3.3 BOUNDARY LAYER THEORY

The theory of Boundary Layers is extremely essential in understanding how the heat transfer due to convection takes place. We shall look at two boundary layers in this section, the *velocity* and the *thermal boundary layer*.

In order to understand the formation of the velocity boundary layer, let us consider the flow of a fluid over a flat plate (Incropera et al.). The moment the fluid particles come into contact with the surface of the plate they experience a sudden friction causing particles immediately adjacent to the surface to have zero velocity, this condition is also known as the no slip condition. With a distance y from the leading edge of the plate, the particles should regain their free stream velocity u_∞ unaffected by the retardation. This gradient in vertical velocity is also known as the *shear stress* τ acting on the fluid.

$$\tau = \mu \frac{\partial u}{\partial y}\bigg|_{y=0} \tag{20}$$

Here μ is the dynamic viscosity which is another fluid property. The velocity boundary layer is characterized by the profile that is created due to the variation of u velocity with distance y as shown in the figure 10.

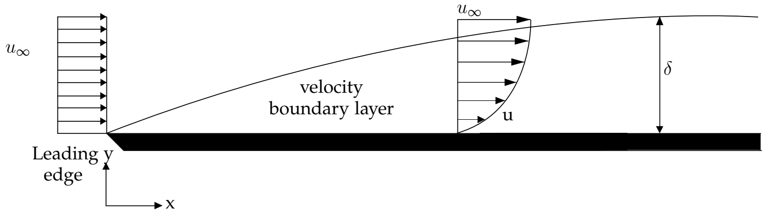

Figure 10: The velocity boundary layer developing from the leading edge of a flat plate

The existence of a *velocity boundary layer* entails that there simultaneously exists a *thermal boundary layer*. The fluid particles in contact with the surface will heat up to the temperature of plate and these particles will in turn exchange heat with their adjacent layers, leading to a gradient in temperature along the vertical direction. Just as in the case of the velocity, at a distance from the leading edge, the fluid temperature will be unaffected by the temperature of the plate returning to the free stream temperature of the fluid T_∞.

$$q_s^{''} = -k_f \frac{\partial T}{\partial y}\bigg|_{y=0} \tag{21}$$

The equation 21 is called the *Fourier's law* evaluated at the surface of the plate. This law states that the heat transfer takes place through conduction with k being the thermal conductivity of the fluid. This assumption can be made by recollecting the no slip condition where the fluid velocity is zero at the surface of the plate.

If there is a difference between surface and free stream temperatures, there will always be heat transfer. This is characterized by the *heat transfer coefficient* given by the relation:

$$h_c = \frac{q_s^{''}}{(T_s - T_\infty)} \tag{22}$$

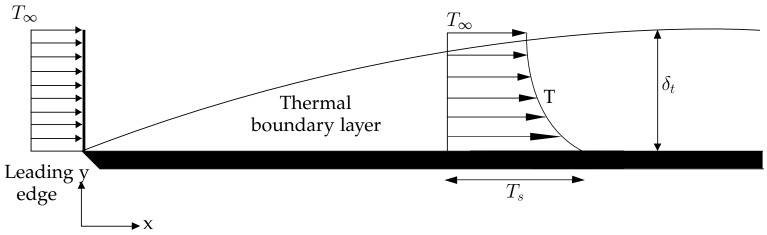

Figure 11: The Thermal boundary layer developing from the leading edge of a flat plate with surface temperature T_s

3.4 INTERNAL FLOW IN PIPES

We have looked at the flow near the leading edge of a flat plate and have characterized the velocity and thermal boundary layers for that case. In case of internal flows or flow in a pipe of circular cross section, there exists a similar boundary layer which is symmetrical about the centre axis (z-axis in most cases). This leads to the formation of a parabolic profile as illustrated in figure 12.

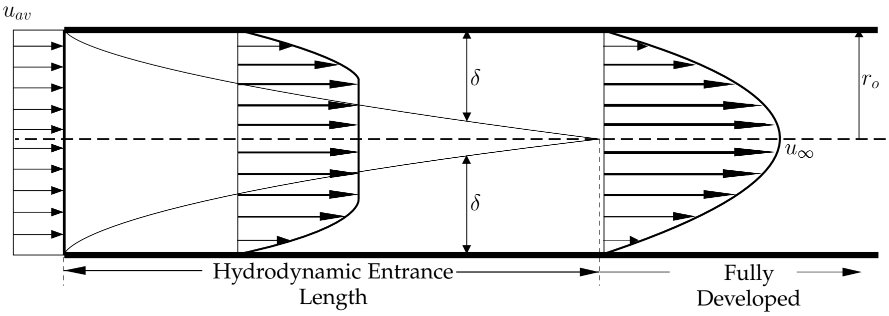

Figure 12: The flow developing inside a pipe

As we go further away from the inlet, the boundary layers from both walls meet beyond which the velocity profile doesn't change for the same cross section of the pipe. This distance from the inlet is called the *hydrodynamic entrance length* and the flow beyond this point is said to be *fully developed*.

We have so far looked at the velocity profiles pertaining to laminar flow. We can introduce the non-dimensional quantity called the *Reynold's Number* given by equation 23.

$$Re = \frac{\rho u_m D_h}{\mu} \tag{23}$$

where u_m is the mean velocity which can be obtained by surface averaging the velocities along the cross section of the pipe. D_h is called the *hydraulic diameter* which is essentially the diameter for a circular cross section. For other shapes it is given by:

$$D_h = \frac{4A}{P_w} \tag{24}$$

here, A and P_w are the cross-sectional area and the wetted perimeter of the flow cross section respectively. The *Reynold's number* gives the ratio of the inertial forces to the viscous forces. When the Re of a flow exceeds the critical value of $Re_{crit} = 2300$ (straight pipe) the flow becomes unsteady and turbulent. The boundary layer is not a parabola any more but becomes flatter after being fully developed.

3.5 PRESSURE DROP IN INTERNAL FLOW

We require the value of pressure drop through a channel for calculating the amount of pumping power required to maintain a steady flow rate. Recalling the basic electric theory, the pressure drop is analogous to voltage drop and the volumetric flow rate, to the current. There will exist a resistance called friction along the length of the pipe but unlike electrical circuits, this resistance varies non-linearly with the flow. The friction factor called the *Darcy friction factor* can be calculated from:

$$f_D = \frac{64}{Re} \tag{25}$$

This should no be confused with the *Fanning friction factor* which is 4 times smaller than the *Darcy friction factor*. Equation 25 can be used to calculate the dimensionless friction in the case of laminar flows in straight circular pipes, for turbulent flows however, exact values have not been predicted due to the random behaviour of the fluid particles but can be estimated to a good accuracy using the *Moody Diagram, Colebrook-White equation* and many more. To calculate the pressure drop we can use the *Darcy Weisbach equation* as shown in eq 26.

$$\Delta p = f_D . \frac{L}{D_h} . \frac{\rho u^2}{2} \tag{26}$$

Where L is the length of the pipe or channel.The longer the pipe, the higher the pressure drop and a wider pipe results in a lower drop. In case of parallel pipes, the pressure drop across all pipes (having the same inlet and outlet height) should be equal (like voltage drop in a parallel circuit) if we considering that there is negligible loss in the splitting region. This relationship is crucial in calculating flow rates from pressure drops in parallel channels that we will deal with later in the chapter.

3.6 APPLICATION OF THEORY

3.6.1 *Air-gap heat transfer*

The behaviour of a fluid between two concentric cylinders has been studied by Childs and Long,Fénot et al. and Howey et al. where they mention that below a critical angular velocity the flow remains a *Couette Flow* which is steady and laminar but beyond this speed there are formation of *Taylor Vortices* which result from instabilities. The critical velocity was given by the value corresponding to a Taylor number *Ta* $\geqslant 41.19$

$$Ta = \frac{\Omega_m r_m^{0.5}(b-a)^{1.5}}{\nu} \tag{27}$$

rearranging eq. 27 to give:

$$\Omega_{cr} = \frac{41.19 \nu F_g}{r_m^{0.5}(b-a)^{0.5}} \tag{28}$$

where F_g is a geometric factor expressed as:

$$Fg = \frac{\pi^2}{41.19\sqrt{S}}(1 - \frac{b-a}{2r_m})^{-1} \tag{29}$$

$$\begin{aligned} S = 0.0571(1 - 0.652\frac{(b-a)/r_m}{1-(b-a)/2r_m}) \\ + 0.00056(1 - 0.652\frac{(b-a)/r_m}{1-(b-a)/2r_m})^{-1} \end{aligned} \tag{30}$$

where ν is the kinematic viscosity of air and r_m is the air-gap radius. Below $Ta^2/F_g^2 \leqslant 1700$ the flow is a laminar shear flow dominated by conduction, for $1700 \leqslant Ta^2/F_g^2 \leqslant 10^4$ the flow is laminar with vortices and $10^4 \leqslant Ta^2/F_g^2 \leqslant 10^7$ the flow is turbulent. After substituting the machine parameters a value of 7424 was found meaning that the flow was laminar with vortices. The corresponding Nusselt number was given by:

$$N_u = 0.128(Ta^2/F_g^2)^{0.241} \tag{31}$$

and the convective heat transfer coefficient h_c between two concentric cylinders of radii a and b can be calculated from:

$$h_c = \frac{N_u.k}{2(b-a)} \tag{32}$$

3.6.2 *End region heat transfer*

Analysing the heat transfer in the end region influenced by the rotation of the rotor is a complex task. Boglietti et al. performed experimental tests and numerical simulations on a *Totally Enclosed Fan Cooled motor* which relies on the heat transfer from the frame to ambient to keep the machine within thermal limits. In the current machine, we have an outer rotor and the entire machine is enclosed by the rotating frame. One side of the machine has small vanes which are connected to the rotor frame but are located slightly far away from the end winding region, the other end region of the machine is enclosed by a small region of air and has no vanes. Taking data from the study by Boglietti and based on the design of the machine, we can expect very little influence of forced convection in the end regions. However since the region is enclosed by a small volume of air, there will be circulating air due to natural convection or *bouyancy* which will play a significant role in heat transfer.

3.6.3 *Outer rotor convection*

There is also a small amount of iron losses generated in the rotor and heat generated from the stator may cross the air-gap and reach the rotor iron. In the test machines, there is a steel rim that is separated from the rotor iron by a small air-gap which has to be included in the calculation. Özerdem performed experiments on a horizontal cylinder rotating in still air and found satisfactory correlations similar to past studies. He makes use of the *Rotational Reynold's number* shown in eqn. 33.

$$Re_r = \frac{\Omega D_o^2 \rho}{2\mu} \tag{33}$$

where D_o is the rim outer diameter, and Ω is its angular velocity. He formulated the relation for Nusselt number based on regression analysis as 34.

$$N_u = 0.318(Re_r)^{0.571} \tag{34}$$

3.6.4 *Cooling Channels convection*

The last convective heat transfer coefficient that needs to be estimated is of the cooling channels. The behaviour of flow inside a curved channel is substantially different from that of a straight pipe. Studies were initiated many years back on flow in curved pipes, a brief review of the various studies undertaken was shown by Piazza and Ciofalo quoting early research dating back to 1908 by Grindley and Gibson. Later many researchers looked into such flows like Eustice in 1911 and Einstein in 1927, but a more quantitative approach was proposed by Dean in 1927 where he explains a shift of the velocity maxima toward the outer wall. This hypothesis was confirmed by scientists like White who conducted experiments and showed a deviation in the resistance to flow in case of a curved pipe and that the point of transition to turbulence did not follow the critical value of that of straight pipes but was a function of a dimensionless parameter called the *Dean Number;*

$$\kappa = \frac{\rho v d}{\mu}(\frac{d}{D})^{\frac{1}{2}} \tag{35}$$

He mentions the presence of secondary circulation effects caused by the pressure gradients owing to centrifugal force. Later Seban et al. quantifies this transition and provides correlations for friction factors in curved pipes adhering within 8% of White's equation. What justifies the need to perform a more detailed analysis into the flow in curved pipes is that the heat transfer coefficient (sought after by us) on the upper wall is higher than in the case of a straight pipe. Thus it is rather important to verify the results of simulations with flow profiles from earlier experimental and numerical studies. Mori and Nakayama provided visual proof of flow patterns as quoted by earlier works and mentions that the additional resistance to flow was due to stresses produced by secondary flow patterns (vortices). Hwang and Chao provided useful insight into the characteristic of this flow in a curved isothermal square duct and mentions the onset of four vortices instead of two under certain initial conditions.

Boundary conditions are required for numerical studies. Of them the flow rates which are dependent on friction factors are important as will be explained in the coming sections. Naphon and Wongwises in his review of flow in curved tubes, shows various correlations for friction factors that have been experimentally proven and provide a good starting point to calculate initial flow conditions. Another important factor is the choice of flow studied, whether laminar or turbulent equations are to be solved. A good quantification of this transitional Re is provided by Piazza and Ciofalo who studied transition to turbulence in toroidal pipes by numerical studies and can be utilized to confirm the type of flow within the machine being studied in this thesis. The section follows with an introduction to *Computational Fluid Dynamics* and how it was used to calculate the heat transfer coefficient we desire.

3.7 WHY CFD?

Partial differential equations have been used for many years to represent the physics of flow and of them the *The Navier Stokes* equations have gained prominence to accurately depict fluid physics. However to analytically solve these set of equations is not a practical approach and thus many have resorted to using scaled models to make use of the advantage of non-dimensional parameters like the *Reynold's Number* which can be reached in many ways to reproduce a larger scaled phenomena. Apart from the extra work required to build scaled models, there is also the disadvantage of trying to recreate all the flow conditions. With technology, measuring equipment has evolved to give accurate readings for parameters like drag and heat transfer coefficients with relative ease, but they still do not manage to give an easy insight into certain in depth phenomena like flow separation and heat contours.

With the arrival of computers, many things changed and more emphasis was put into computerizing fluid mechanics. By using a method called discretization we can convert partial differential equations to an array of algebraic equations that can be iteratively solved by a computer with ease. As simple as that sounds, there is still a lot of complexity involved with approximating partial differential equations for more complex geometries and scenarios.

3.7.1 *The Numerical Simulation Procedure*

The very first step to any numerical simulation is the **mathematical equations** describing the type of flow being investigated. The next step is to discretize the partial derivatives into algebraic approximations. There are different types of methods but the three well adopted ones are the *Finite Difference (FD)*, *Finite Elements (FE)* and the *Finite Volume (FV) Methods.* They follow different approaches but tend to the same solution as space and time reduce close to zero (Tu et al.).

Let us see an example of how to discretize a simple one dimensional time dependent equation which appears in radio-active decay, cooling of an object etc.

$$\frac{dT}{dt} = -KT \tag{36}$$

We can assume a one dimensional grid with uniform spacing of Δt (in our case we are discretizing in time) and with temperatures T_i at each point. Then we can approximate the partial differential equation by assuming a linear profile between two points as:

$$\frac{dT}{dt} \approx \frac{\Delta T}{\Delta t} = \frac{T_2 - T_1}{\Delta t} = -Ky \tag{37}$$

We can assume the right hand side temperature to be T_1 (explicit) or T_2 (implicit) giving:

$$T_2 = T_1(1 + K\Delta t) \tag{38}$$

and in a generalized expression :

$$T_{new} = T_{old}(1 + K\Delta t) \tag{39}$$

The same method can be applied to a one-dimensional heat transfer case governed by the equation 40 :

$$\frac{\partial T}{\partial t} = \alpha \frac{\partial^2 T}{\partial x^2} \tag{40}$$

The one dimensional space is be made of N discrete points separated by a distance Δx as shown in fig 13. Each element is the region between two nodes, this is where the parameters like temperature etc.

are defined. At the left end of the region we prescribe the temperature to be 0 °C and at the right, to be 20 °C. These values that we impose on the regions are called the *boundary conditions*. We require linear approximations of the partial differential equations that are calculated at each cell. For point 1, the same time derivative described in the previous section is used, but for the second order spatial derivative we have to perform one more step. The first differential in space for the point 1 and 2 is:

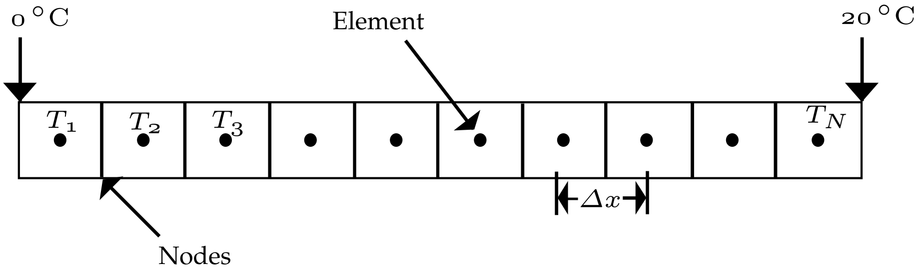

Figure 13: A one-dimensional grid

$$\frac{dT}{dx} = \frac{T_2 - T_1}{\Delta x} \tag{41}$$

Similarly, we can consider the second differential to be the differential on the differential at points 1 and 2 individually. We however run into the problem that since we consider the first cell to have the subscript 1, we cannot find the differential with respect to the previous point (No zero cell). This can be solved with inserting what is called a virtual cell (Fig.14). Now that we have points 0, 1 and 2, the linear approximation of the second order spatial derivative at point 1 is:

$$\frac{\partial^2 T}{\partial x^2} \approx \frac{\frac{T_0 - T_1}{\Delta x} - \frac{T_1 - T_2}{\Delta x}}{\Delta x} = \frac{T_0 - 2T_1 + T_2}{\Delta x^2} \tag{42}$$

The time and the spatial derivative temperatures are separate and have to be denoted by different subscripts to avoid confusion. Combining the two derivatives and generalizing the subscripts we obtain equation 43.

$$T_{new} = T_{old} + \frac{\alpha \Delta t}{\Delta x^2}(T_{i-1} - 2T_i + T_{i+1}) \tag{43}$$

The T_{new} is the new time level and the T_{old} is from the previous iteration. This overwriting of time values saves memory. In a real geometry, the temperature would be prescribed on the wall i.e. the nodes, but we calculate the values from the cell centres. This can be compensated by either changing the type of mesh to include one point on the end walls, or to make use of a virtual cell as described earlier. This virtual cell value has to be constantly updated based on the boundary condition by assuming a linear profile in between cells.

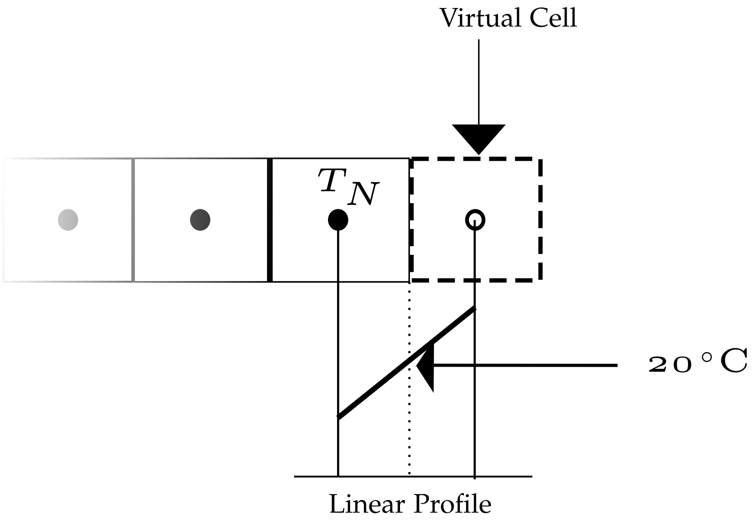

Figure 14: A virtual cell at the right end of the grid

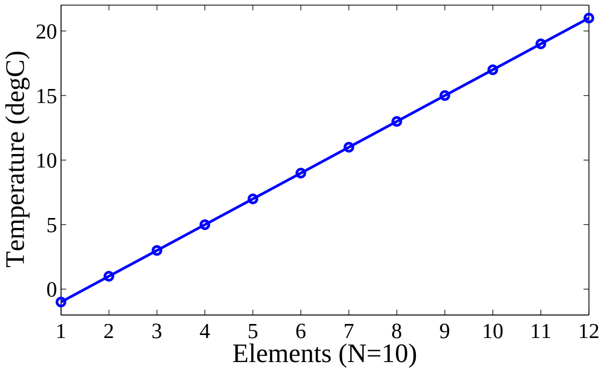

Figure 15: A one-dimensional heat transfer solution in MATLAB

$$T_{virt-left} = 2T_L - T_i \tag{44}$$

and at the right end as:

$$T_{virt-right} = 2T_R - T_N \tag{45}$$

Solving these equations with a nested loop, one for time and the other for space, in an iterative process, it gives rise to the simple solution as shown in Fig.15. This way of solving the equation is called the *Method of lines*. There are 10 grid cells with two virtual cells on either end. The boundary conditions are prescribed between the virtual and end cells i.e. the end nodes.

The solution shows a linear temperature profile similar to what would happen to a rod with temperatures at both ends. There are always errors in the final solution and the stability of this method strongly depends on the step size, grid spacing and the material

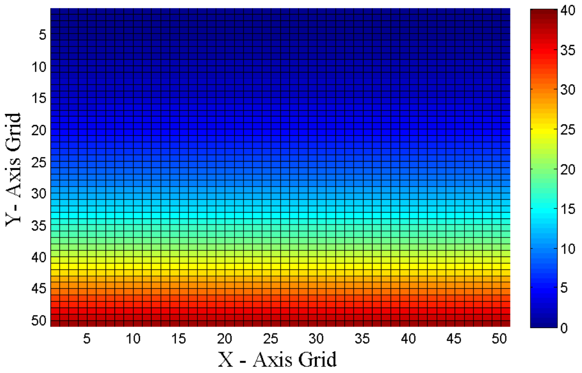

Figure 16: Two-dimensional temperature surface contours in MATLAB

property alpha. With little modification to the previous example, a two-dimensional in-stationary heat transfer problem can be solved (equation.46). This would yield a solution as shown in Fig 16 calculated on a 50 by 50 grid.

$$\frac{\partial T}{\partial t} = \alpha(\frac{\partial^2 T}{\partial x^2} + \frac{\partial^2 T}{\partial y^2}) \tag{46}$$

The plot represents a two-dimensional rectangle that is heated at the bottom edge to 40 °C with the top edge at 0 °C. The solution was stopped before attaining the final solution due to the computational time of this simple solution. The restrictions on time and accuracy led to the development of more advanced solvers and approximation methods. We shall look at a few later on in the chapter.

There are different methods of meshing that can be applied to also irregular geometries. A structured mesh is an ordered grid where each point is linked with the other neighbours in a uniform manner as shown in figure 17.

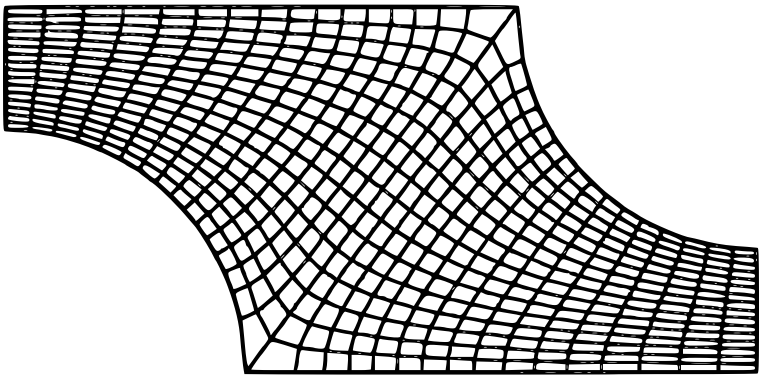

Figure 17: An example of a structured mesh

They suffer from the drawback that the regions where mesh density is required to be high cannot be refined without effecting the surrounding cells, leading to an overall higher dense mesh which can be a waste of resources. Another type of grid is the unstructured grid which is as the name states, not as uniformly oriented like in the former case. Despite the lack of uniformity, unstructured meshes can be applied to more complex geometries and can be separately dense where required as shown in figure 18. The downside to having this type of grid is that the connectivity has to be explicitly defined and stored. There are other types of meshes which are beyond the scope of this thesis.

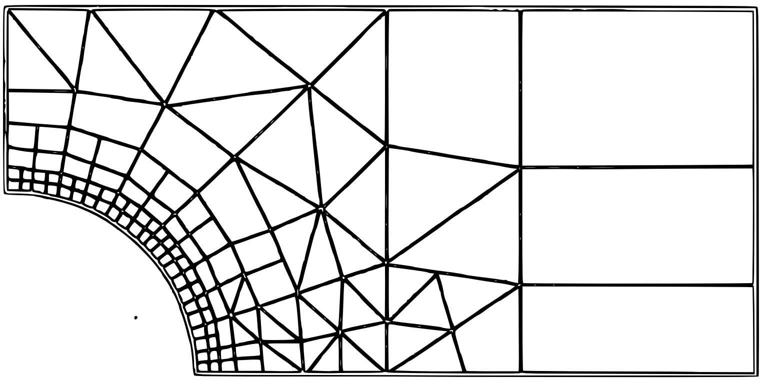

Figure 18: An example of an unstructured mesh

The method of solution is also of utmost importance for it defines the stability and accuracy of the solution being sought and the choice of the solver usually depends on the problem. A direct solver uses Matrix Elimination procedures to solve the system Matrix (e.g. Gaussian Elimination), while an iterative solver computes the solution based on certain predictions (e.g. Gauss-Seidel). The former has the advantage of being able to deliver a solution even with an ill-conditioned matrix but at the risk of more memory consumption. The latter consumes much less memory, but might not guarantee convergence for all problems.

3.8 SIMULATION OF A CIRCULAR CROSS SECTIONAL PIPE

We first simulate a simple curved circular pipe to compare with the majority of literature, once we can obtain similar results, we can move on to the channels of the machine.

3.8.1 *Meshing and Boundary Conditions*

The meshing was carried out in Ansys ICEM CFD using a blocked mesh approach with hexahedral cells. The method of 3D mesh generation was sweeping which can be done well on long geometries that do not change shape with length. The general rule is that the mesh should more or less represent the geometry of the flow region and should be smaller in regions where there is expected to be large gradients in flow parameters like velocity, temperature etc. If we recollect the theory from earlier in the chapter we see that the boundary layer formed within a pipe has large velocity gradients near the wall and in order to calculate the shear stress (τ_w) at the wall accurately, a finer mesh is required. We expect to simulate the effects of a helical flow of fluid particles and hence care should be taken to allow for the calculation of changes in the axial direction, this can be done by using a finer mesh over all throughout the cross section of the pipe. Once the mesh is designed based on this basic knowledge of the physics, a mesh convergence test should be done. This means that the mesh is made finer till the results (especially the parameter we require most) does not change with further refinement. The mesh of the circular cross section pipe is shown in Fig. 19.

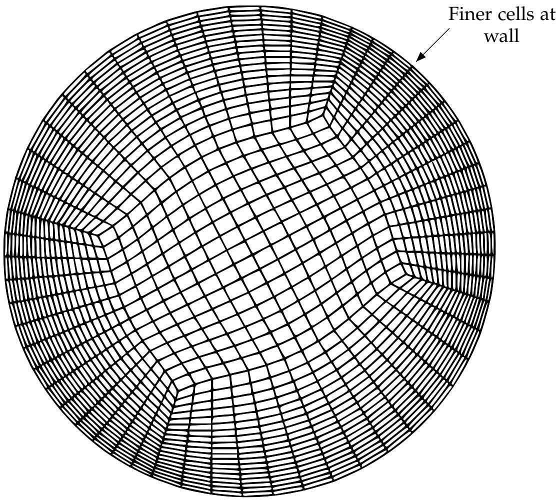

Figure 19: Mesh of pipe cross section

After the mesh has been generated in ICEM, the ANSYS Workbench transfers the work flow to FLUENT a popular CFD software. Here the quality of the mesh can be further assessed, and this mesh was tested for a quality of 0.7 out of 1 which is good. The type of simulation and models were *3D steady* and *viscous laminar* and the type of solver was the *Pressure-based Navier Stokes solver*. The material was provided to the fluid cell zone as 50% Ethylene-Glycol with material properties taken at 60 °C. The inlet condition was mass-flow with a value chosen to give a velocity close to 1 m/s for this cross-section and the outlet was *pressure-outlet* with a gauge pressure of zero pascal. Finally the wall was given a *no slip* shear condition as discussed earlier in the theory section.

3.8.2 *Simulation and Post Processing*

The criteria for completion of the simulation is when the error between consecutive iterations reaches a specific user defined value called the *Convergence Criterion*. The criteria for this simulation was set to 0.001. In our case we can stop simulations when the shear stress at the wall no longer changes with each iteration thus indicating user defined convergence of the solver variables we are interested in.

Post-processing can be done within FLUENT itself and allows you to visualize the solutions calculated by the solver. Fig. 20 shows the velocity contours at the outlet of the pipe which are very similar to those quoted in literature. There is a shift of the velocity maxima towards the upper wall of the channel due to centrifugal effects.

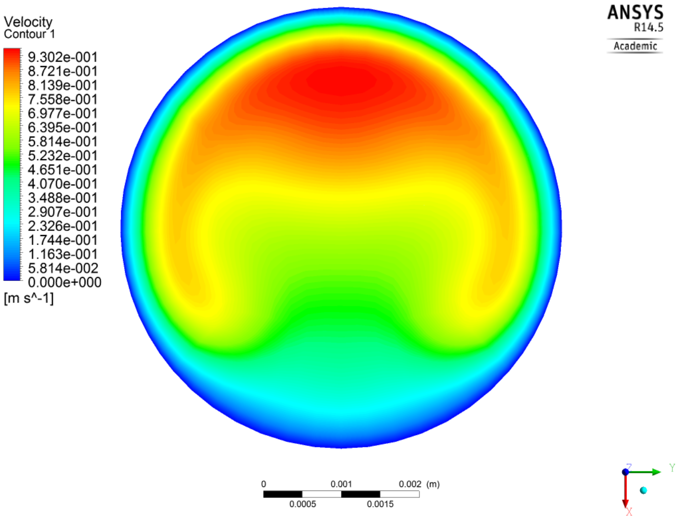

Figure 20: Velocity profile of pipe cross-section

The fluid particles being pushed to the top of the pipe will begin to circulate on account of the boundary. This causes what we have discussed earlier called the Dean vortices. A clearer depiction of this velocity profile can be seen from the Fig.21 that shows it's vectors at the outlet.

3.9 SIMULATION OF THE ORIGINAL CROSS SECTION

The results obtained from simulating a circular pipe help justify the type of simulation configurations and mesh structure that can be used to include the effect of secondary flow. Now can utilize the same configurations on the original cross-section.

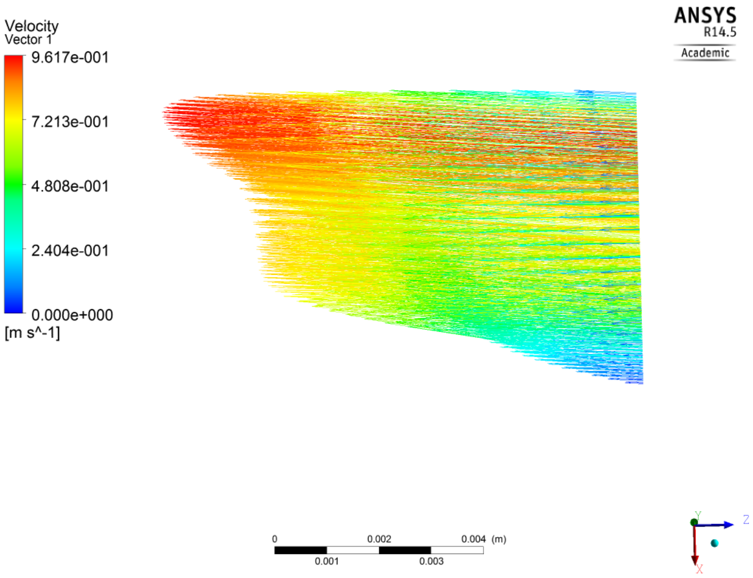

Figure 21: Velocity vectors at outlet seen normal to the flow from the side

3.9.1 *Geometry Conditioning*

The geometry of the cooling channels were shown in Chap.2, but it cannot be directly used for CFD computation. Using a Computer Aided Design (CAD) approach, we can condition the geometry making it mesh-friendly. Complex shapes and curves which do not effect the flow to a reasonable extent can be removed to reduce the number of elements of the mesh. The flow region can be extracted from the machine as shown in Fig.22 to be simulated separately conserving resources.

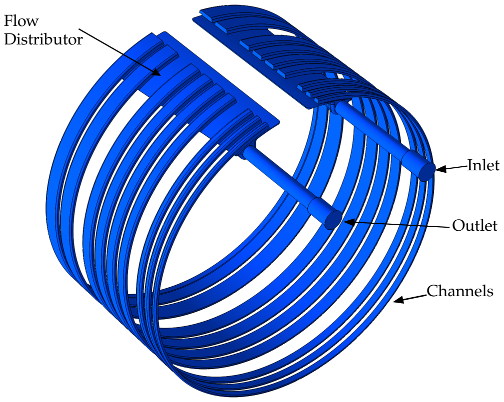

Figure 22: Extracted flow region using CAD software

The cooling channels have a common inlet region which distributes the flow amongst the nine channels. Ideally flow distribution regions are constructed to equalize pressure and thus if proper assumptions are made for the flow in the individual channels, this complex shape can be removed from simulations. The final geometry is shown in Fig.23 where only the nine channels are shown. It must be noted that the inlet distribution region may have an effect on mass flow and over all pressure loss, but due to the complexity of the geometry it will not be taken into account.

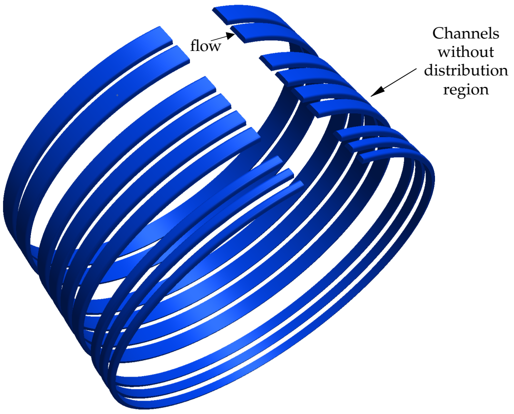

Figure 23: Simplified flow region

It is important to preserve the shape of the channel walls as they will play a vital role in how the secondary flow will be developed. The channel dimensions are given in a separate chapter.

3.9.2 *Meshing and Boundary Conditions*

The channels were meshed respecting the same set of requirements as mentioned in the previous section. The meshes near the walls were more dense than that at the centre and the over all mesh density was chosen to be higher than that of a straight pipe. In reality there are nine channels sharing a common inlet and thus there will be a division of flow among the channels in a ratio proportional to their flow resistances. We neglect the pressure drop in the inlet region and thus we know that the pressure drop is equal across parallel channels. The Darcy Weisbach equation written as a function of volumetric flow rate is:

$$\Delta P = f_D.\frac{L}{D_h}.\frac{\rho Q^2}{2A^2} \tag{47}$$

Where f_D is the Darcy friction factor for flow in curved pipes for which we utilize White correlation. We also know that the sum of the individual flow rates is equal to the total flow rate at the inlet given by

$$Q_T = \sum_{i=1}^{9} (Q_i^2) \tag{48}$$

Thus by iteratively solving both these equations, we can calculate the individual channel flows and Reynold's numbers using the *pipe Reynold's number formula* (49) as shown in table 6.

$$Re_D = \frac{\rho u D_h}{\mu} \tag{49}$$

D_h is the hydraulic diameter, ρ is the density and μ is the dynamic viscosity of the fluid.

Channel No.	**Mass flow rates (kg/s)**	**Dean No.**	**Reynold's No.**
1	0.008	90	710
2	0.0098	105	800
3	0.0117	118	880
4	0.0216	170	1180
5	0.0236	180	1230
6	0.0258	187	1270
7	0.0279	195	1310
8	0.0364	218	1450
9	0.0386	225	1475

Table 6: Calculated flow parameters from MATLAB

From our earlier knowledge of flow transition in curved pipes, we can confirm that the Reynold's number is well within the transition region and thus **laminar flow equations can be used**. The channels were simulated individually due to restriction in the computational resources available. The inlet boundary was given a *mass flow* condition and the outlet was a *pressure outlet*. Since we fundamentally require the values of heat transfer coefficient, in addition to solving the *laminar-viscous* model, we also activate the *Energy* model in FLUENT to enable temperature definitions. The upper wall of the channel is given a prescribed temperature of 400K together with the *no slip* condition. And the fluid material was chosen accordingly with properties as mentioned earlier.

3.9.3 *Simulation and Post-Processing*

There was difficulty in obtaining a convergence on a steady solver because of which a time-dependent solver was used (more stabil-

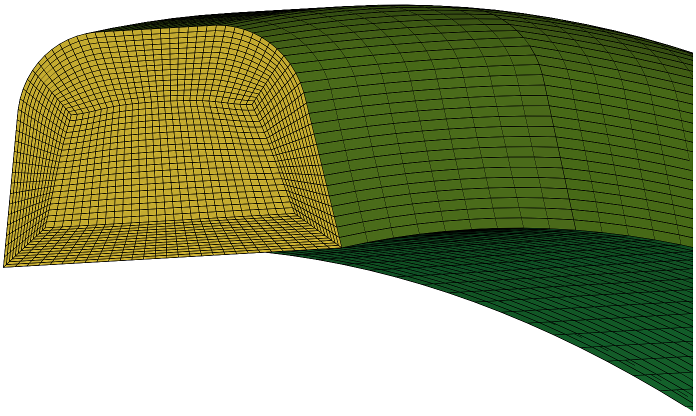

Figure 24: Mesh of the first channel in ICEM-CFD

ity). The convergence error tolerance was set to 10^{-5} to fully capture the effects of secondary flow and the time step was calculated accordingly to ensure temporal convergence. Despite preforming an unsteady simulation, the physics eventually will reach a steady state and convergence time will reduce with each time step.

The results for each channel were different in terms of the flow profile (various aspect ratios) and vortices were clearly distinguishable at larger channels. The heat transfer coefficient was calculated using (22) using a reference value of 45 °C. There were variations of the value of this heat transfer coefficient along the length of the channel because of an under-developed flow region and the presence of circulation effects (Fig.27,25), thus a surface averaged value based on the area of the outer wall (where temperature is prescribed) was calculated as the generalized value for a particular channel shown in table 7. The temperature of the fluid adjacent to the wall was at its temperature and the hot fluid at this region starts circulating to the centre of the channel carried by the vortex effect. This results in a much better mixing of fluid and higher shear stresses on the outer wall in the case of curved flow.

The figure above shows the diverse characteristics of the flow in the nine channels. Due to a higher flow rate the centrifugal effects on the channels increase with increasing number. Nevertheless there are predominant circulatory effects even under low flow conditions due to the radius of curvature. They are more clearly differentiable in Fig.

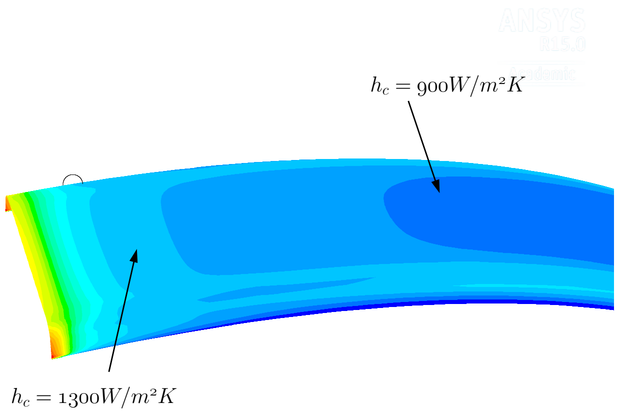

Figure 25: Heat transfer coefficients at entrance

channel 1

channel 4

channel 9

Figure 26: Velocity contours for three different channels

28 where fluid particles reaching the top wall follow the curvature of the wall in a helical fashion.

The temperature of the fluid was colder at the eyes of the vortices where the fluid wasn't being displaced and patterns shown in Fig 29 are crucial in confirming the circulation effects. On channel 9, we see

Channel No.	Heat transfer coefficient h_c (W/m^2K)
1	684
2	707
3	748
4	754
5	770
6	787
7	802
8	857
9	868

Table 7: Heat transfer values calculated as the surface average

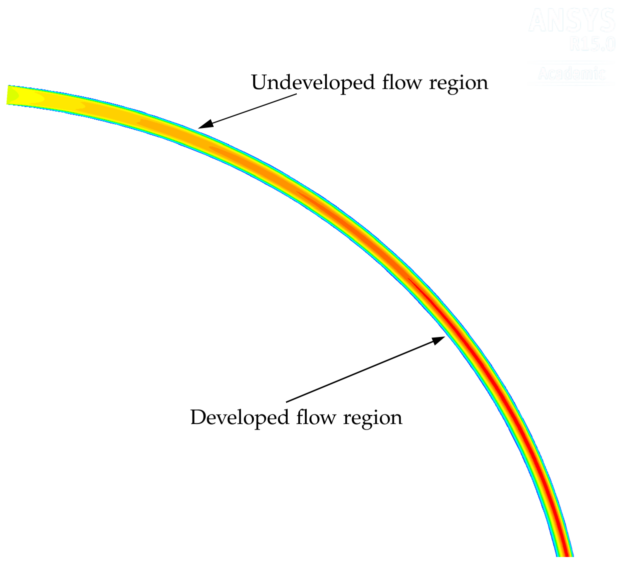

Figure 27: Velocity contours showing developing flow

a new pair of eyes at the centre of the channel which can be expected due to the large aspect ratio of the channel.

3.10 CONCLUSION

The various studies performed by different scientists was presented which served as a basis for verification of the results. There were also two pairs of vortices spotted in the larger channels which indeed strengthens the fact that flow in curved pipes are very dependent on the shape of the channel and that care has to be taken during meshing and convergence to be able to simulate secondary flows. With this

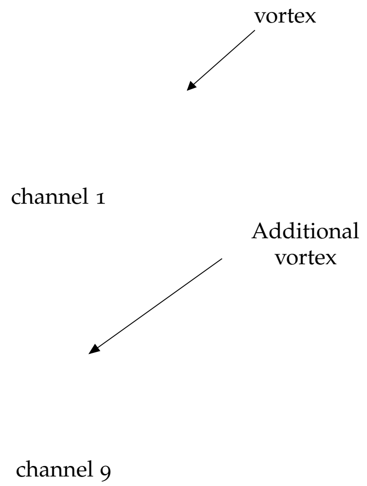

Figure 28: Velocity vectors for three different channels

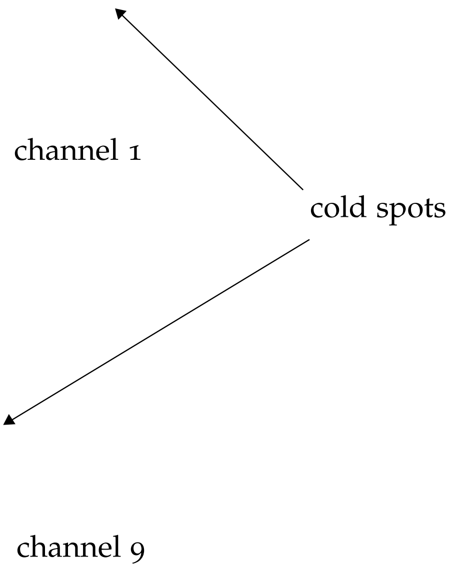

Figure 29: Temperature contours for two channels

value of heat transfer coefficient and the other convection parameters obtained earlier, we now have the various boundary conditions to proceed with the heat transfer simulations.

4

THERMAL MODELLING

So far we have calculated the various thermal resistance values and convection coefficients relating to the machine. Till now, the procedure followed is common to any modelling technique, analytical or numerical but we exploit the advantages of using the latter, particularly the Finite Element Method for solving the heat transfer problem at hand.

4.1 OBJECTIVE

The main goal of the thesis was to derive a single model that can reproduce the machine hotspot and use the results of the model to identify methods to reduce temperatures. The required parameters like heat transfer coefficient, air-gap thermal resistances etc. were identified in the previous chapters and can now be integrated into a single simulation. The following sections describe the comparison of the results of the model with experimental data obtained from a test bench.

4.2 THE FINITE ELEMENT APPROACH

In chapter 3 an introduction to numerical modelling followed by a general procedure was explained. We shall follow the same procedure for performing the heat transfer simulations as well. The software used was COMSOL 4.4 a very capable tool for finite element analysis in which the work-flow of modelling is as follows:

1. Geometry import/creation.
2. Choosing the appropriate physics models (equations)
3. Meshing
4. Choosing a solving method.
5. Post-processing the result

This may look very familiar to the computational fluid dynamics simulations from the previous chapters. Since the description of the methods were already given, we shall dive directly into the execution.

4.2.1 *Geometry import/creation*

The geometry is simplified using the CAD software *Solidworks*. The machine is axi-symmetric along the central axis and thus only the repeating pattern needs to be simulated. Half a slot and tooth are selected as the pattern and are sliced out from the 3 dimensional machine geometry. The 2d view of the geometry is shown in figure 30 where the various materials are described by separate domains. This body is then imported into COMSOL and built as an assembly. This option allows physics and material definitions on individual parts.

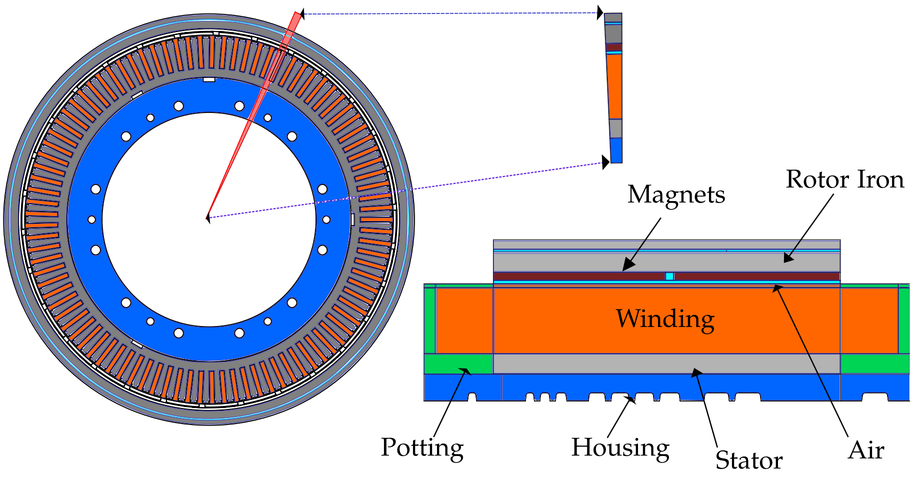

Figure 30: Slice of the machine selected as the geometry for computation

4.2.2 *Problem definition and Physics Models*

The PMSM machine under study has multiple sources of heat each being dominant under certain operating conditions. These sources would cause a temperature rise within the machine in regions where the thermal resistances are high, the objective of this model is to simulate these hotspot regions as best as possible to enable improvements to be made. The physics that deals with this primary objective is the *Heat Transfer in Solids module* provided in COMSOL whose fundamental equation for conduction is given by 50. This equation is valid for a heat source Q on a solid domain with thermal conductivity k and specific heat capacity C_p leading to a time varying temperature T.

$$\rho C_p \frac{\partial T}{\partial t} + \nabla.(-k\nabla T) = Q \tag{50}$$

Each part is linked with the other through a *Continuity Pair* condition. The geometry consists of half a tooth and slot because the entire machine can be represented by repeating its mirror. Some materials in the machine show anisotropy of thermal conductivity and have to be

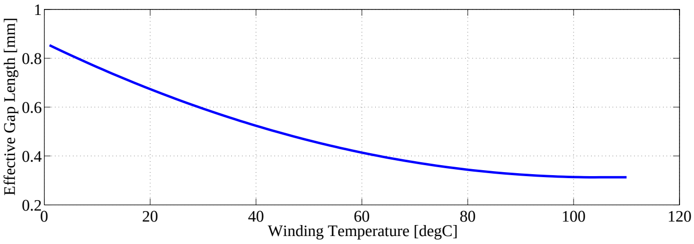

Figure 31: Variation of the equivalent air-gap between the slot liner and stator core

additionally defined at each domain based on cylindrical/Cartesian coordinates. The heat sources are defined on the winding composite and the stator (Copper an Iron losses).

The windings were represented by a rectangular region covering the volume of the slot, the thermal conductivity along the length of the slot was given to be that of the copper, and the other two dimensions were given the value of effective thermal conductivity.

The convective heat transfer coefficients are applied as boundary conditions at the respective channel faces of the housing and the outer rim, this will add an outflow of heat flux based on the relation:

$$q = h_c.(T_{ext} - T_s) \tag{51}$$

where the T_{ext} is the fluid temperature. This value varies with time and hence to get an appropriate value, experimental data for fluid temperatures have been used. In COMSOL functions can be defined as boundary conditions. The convective heat flux boundary is also applied to the end winding potting region specifying *natural convection*. COMSOL allows you to specify the type of boundary (vertical wall, horizontal wall upside and horizontal wall downside) along with the dimensions to internally calculate the necessary heat transfer coefficients.

The various interface gaps are realized using the *Thin Thermally Resistive Layer* option which allows you to specify the thickness of a material with specific thermal conductivity. The temperature variation of the effective air-gap thickness was given as a function of the hotspot temperature for the slot liner air and the fluid temperature for the aluminium-housing air gap as shown in the figures 31 and 32.

The change of copper resistance with temperature can be well defined by adding another physics into the computation, *Electric Currents*. The RMS current value can be specified using a *Terminal* condition that flows through the domain till the face where the *ground*

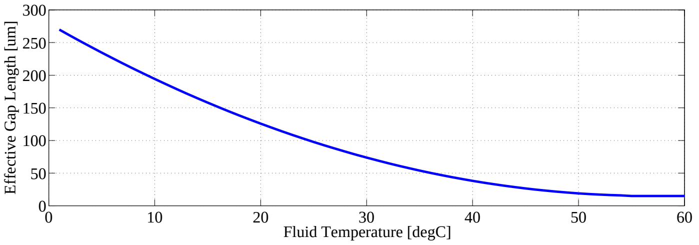

Figure 32: Variation of the equivalent air-gap between stator core and the coolant housing

is specified. The *Linearized resistivity* option must be enabled in the current conservation settings. COMSOL links these two physics and couples the computed parameters internally.

4.2.3 *Meshing*

It was shown earlier that the temperature was calculated at each cell, so the more the cells, the more a gradient in temperature can be mapped. A region of low thermal conductivity has a larger temperature drop across it, and thus a finer mesh is sometimes required to capture this variation. In simple scenarios where the thermal conductivity is isotropic, the temperature would vary linearly across the material and lower cells can be used. The geometry was meshed with bricks because of the rectangular shape of the geometry. The thermal conductivities varied in two axes and could be captured well by the use of the rectangular cells. The domains were individually swept and so had disjoint meshes, but the *Pair continuity* boundary conditions imposed during the physics stage ensures that the two domains are linked at the interfaces during computation.

4.2.4 *Solving*

The choice of solver influences the accuracy and time required to obtain a solution. A direct solver was utilized due to restrictions in time and availability of sufficient RAM. There were two types of solvers used for the study, a stationary and a time dependent one. The initial conditions are rather important for the time dependent solver for they decide the temperature after a particular interval. The stationary solver does not have strict rules about the initial conditions or the density and heat capacitances of the materials.

4.3 SIMULATION RESULTS AND VALIDATION

The final stage is analysing the results obtained from the simulations and validating whether the model reacts realistically. This topic is

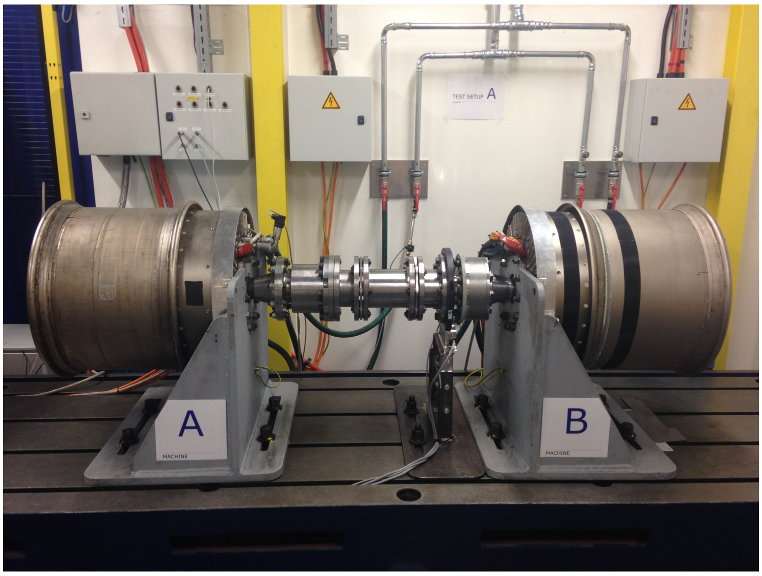

Figure 33: The two coupled machines

large by itself and will be explained in detail in the sections to come. The results are shown in comparison to experimental data and hence the test apparatus is first described before displaying the model results.

4.3.1 *Test set-up*

Experimental results were obtained from a test-bench at the company. Two machines were coupled back-to-back using torque limited coupling rings. The set-up can be visualized in Fig. 33. There were Platinum resistor thermometers (PT-100) located within the end regions of the windings in each of the three phases. They have a temperature range of -50 °C to 230 °C. One of the machines can be run in a Speed control mode while the other runs on a current control. This enables the user to operate one machine at any current and speed within its rating. The inlet and outlet fluid regions had flow and temperature sensors as shown in Fig 34 which were connected to a Portable Data recorder (HBM).

4.3.2 *Steady State Simulation Results*

The simulation was performed initially for 150A at a rotational speed of 50rpm. The iron losses at that speed were rather low compared to the copper losses in the slot and were neglected from the calculation. The temperature contours are shown in fig 35 that show the hotspot regions located at the end windings.

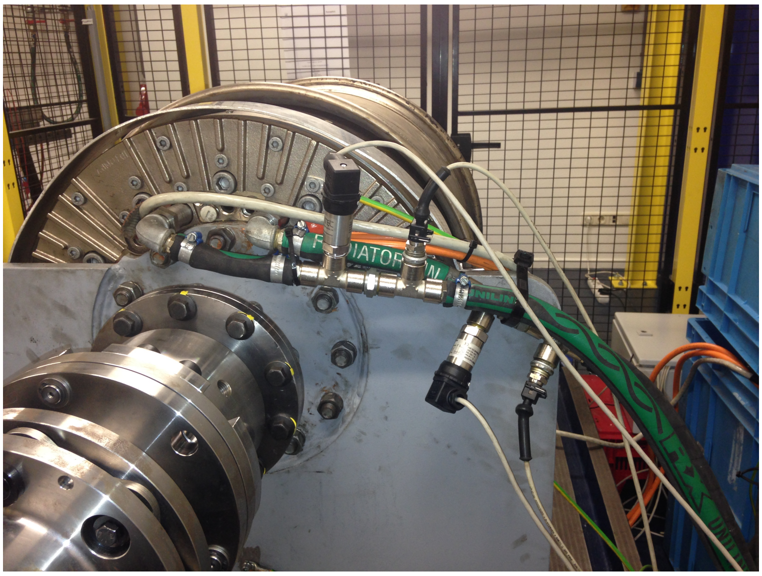

Figure 34: Inlet and Outlet fluid sensors

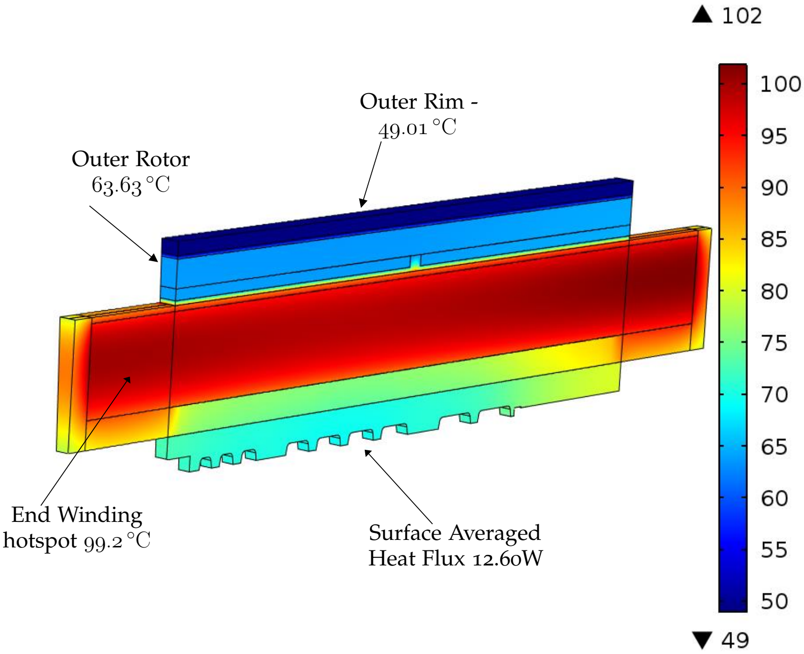

Figure 35: Steady state simulation temperature contours in °C

The temperature was also taken at the rotor's top face and the rim using two sensors, an infra-red sensor and portable PT-100 sensor which was immediately placed when the machine was switched off. The various temperatures are shown in the table below.

An important parameter at hand was the fluid temperature rise between the inlet and the outlet which could be interpreted as the heat flux entering the fluid based on the simple equation 52.

Location	Temperature (°C
End Winding	96.5
Rotor Face	62
Rim Face	48.2
Inlet Fluid	58.71
Outlet Fluid	61.58

$$q' = m_{rate}.C_P.\varDelta T \tag{52}$$

By substituting the properties of Ethylene Glycol at the corresponding average fluid temperature, we can obtain the value of heat flux to be around 11W per half slot for a 2.8 °C rise in temperature between the inlet and the outlet. The total power entering the fluid is divided by twice the number of slots to obtain the value per half slot.

The temperature error between the experiment and the simulations were about 2.7% and for heat flux was around 14%. The significantly larger error in heat flux may be due to inexact values of end-winding heat transfer coefficient or due to the heat leakage through other paths not included within this geometry. However this steady state result provided valuable data into choosing some specific parameters which were under question in the research stage like the steady value of inter-facial air gaps.

4.3.3 *Time-dependent Simulation Results*

There were six sets of experiments conducted that were chosen to exhibit diverse temperatures in the fluid and winding to offer a wider range of comparison as shown in table 8. The initial temperatures were noted at the start of the experiment and the flow rate was fixed to 11 lit/min.

Current (A)	Speed (rpm)	Fluid Temperature Range °C	Time of Test (s)
180	50	20 - 30	1800
180	350	25 - 40	1800
200	50	30 - 50	1800
200	350	40 - 60	1400
180	50	20 - 50	3000
500	<30	-	60

Table 8: Transient test ranges

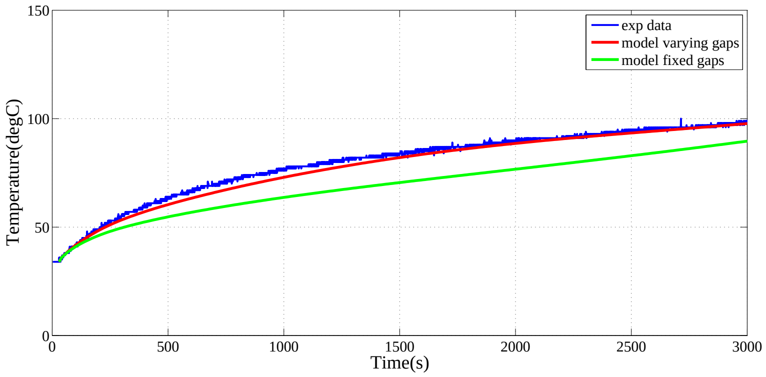

Figure 36: Comparison of Model vs Experiment 180A/50rpm

The model was initially run with the effective inter-facial air-gaps fixed. The model showed a different dynamic behaviour at the early stages and slowly closed in on the experimental value meaning that there is a higher value of thermal resistance at lower temperatures that reduce as the machine heats up, supporting the idea of having a time varying interface gap. Fig.36 shows the behaviour of the model with and without this variation.

The interface between the Aluminium and housing had a much smaller influence in comparison to that of the slot liner. This may partially be explained because of the large differences in thermal expansion ratios between the materials in these two regions. Nevertheless the addition of this function did not cause any delay in simulation and was thus included further on. Using generalized functions to represent dynamic changes in thermal resistances of the machine, the model was simulated by just changing the current at the terminals and addition of extra iron losses taken from the parallel thesis, the results are shown below.

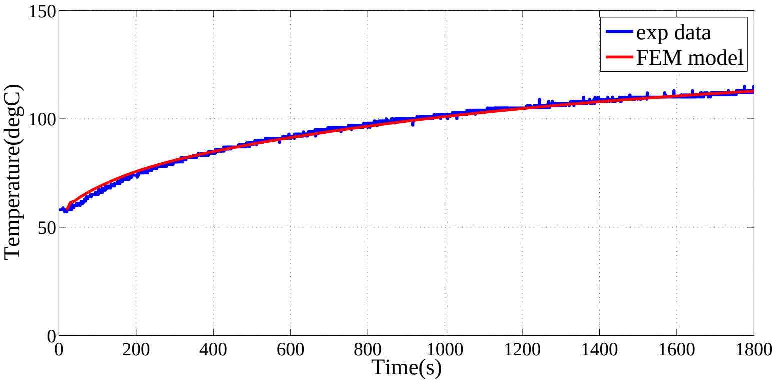

Figure 37: Comparison of Model vs Experiment 200A/50rpm

4.3.3.1 *High Current Transient Test*

The model was expected to also simulate the behaviour of the machine in short periods with high currents. These conditions are very common in electric vehicles especially large ones when driving on slopes with load. The test was conducted for a short period to prevent exceeding the test-bench thermal limits and the fluid temperatures did not see much of a rise in this period and hence was maintained constant in the model. The figure 40 shows the behaviour of the model with experimental results. Both show similar slopes if compared a few seconds after the start of the test, however the initial dynamic response due to thermal inertia could not be reproduced in the model. Despite the initial few seconds, the model predicted the temperature within 5% accuracy of the experiment.

4.4 SENSITIVITY ANALYSIS

A sensitivity analysis was performed on the steady state results at 200A at 50rpm. Steady state simulations predict the highest possible temperatures in time and thus may be higher than in reality with a

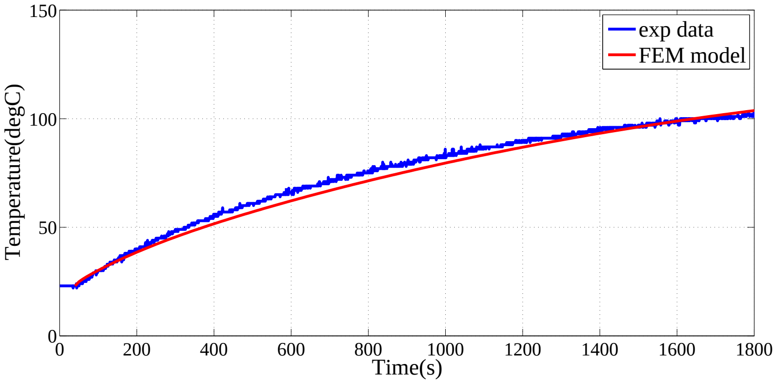

Figure 38: Comparison of Model vs Experiment 180A/350rpm

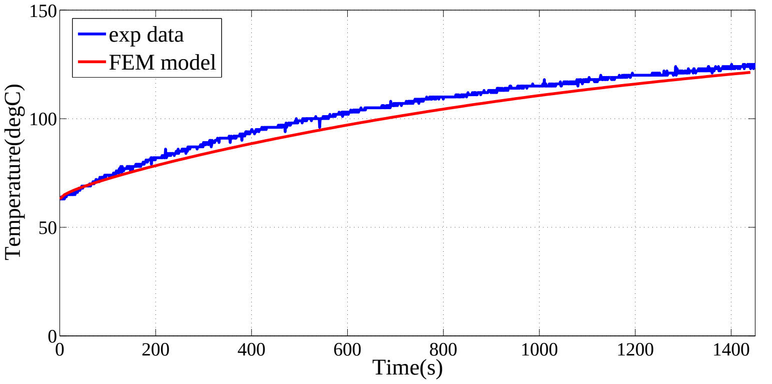

Figure 39: Comparison of Model vs Experiment 200A/350rpm

finite time scale. An automatic parameter sweep could not be performed on a time dependent simulation because of the long computational times. The parameters swept are the heat transfer coefficients at the end winding regions, the interface gaps, thermal conductivity of the potting compound and the value of heat transfer coefficients at the cooling channels. All parameters were varied +/- 50% or +/- 100% to perform this analysis.

Parameter	Sensitivity	Slot max °C	Magnet °C	Heat to Channels W
Default Values	-	135	79.24	26.33
Housing	+50%	139	81	26.242
Air-gap	-50%	131	76	26.40
Slot-liner	+50%	144	79.4	26.63
Air-gap	-50%	126	76	26
Fluid	+50%	128	74	26.24
h_C	-50%	162	95	27.63
Equivalent k of	+100%	133	79.07	26.21
winding	-100%	166	82	27.916
End Winding	+100%	135	79.01	27.169
h_C	-100%	138	80	25.2

Table 9: Sensitivity Analysis on crucial parameters for 200A at 50rpm

From table 9 is it very clear that the end winding heat transfer coefficient has a little effect on the machine temperatures but has the most influence on the power transferred to the fluid. A keen point to be noted is the mass flow rate's influence on the temperature which

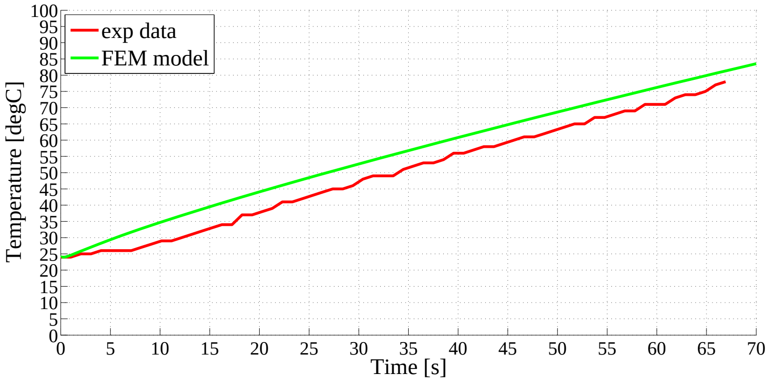

Figure 40: Comparison of Model vs Experiment 500A for 60 seconds

seems advantageous at first but as flow increases further it's influence would decrease, out-weighing the cost of pumping. This analysis gives us an insight into which parameters must be looked into in more detail and this forms the basis for the next chapter that looks into methods to realize these improvements.

5

HEAT TRANSFER ENHANCEMENT

This chapter deals with methods to reduce the temperature of the hot regions within the machine. The effect of changing the potting compound and redesigning the coolant housing will be discussed.

5.1 OBJECTIVES

The availability of a numerical model makes it much easier to view the influence of design changes that are suggested. We have seen from the previous chapters that the copper windings where heat is being generated, is surrounded by an impregnating material. This material has a comparatively low thermal conductivity meaning that a higher temperature drop will occur between the windings and the stator. An air-gap is predicted in the region between the slot liner and the stator making matters worse. In view of that, this chapter focusses more on the variation of the impregnation material and techniques to by-pass or lessen the influence of the parasitic air-gaps.

5.2 PARAMETERS AND OPERATING POINTS

There should be certain regions of operation where the effects of parameter variations can be compared. The continuous operation of the machine under the rated current is an important operating region that can be used for the analysis. Another scenario that may occur in electric vehicle operation is high torques for a short period. This translates to a short time of very high currents. To simulate this scenario, a current of 750A is applied for 30 seconds.

Both these operating points will be compared for the following parameters:

- 5.3 Variation of equivalent thermal conductivity of the slot
  - 5.3.1.1 Current design
  - 5.3.1.2 Extended coolant housing
  - 5.3.1.3 Extended coolant housing with channels
- 5.4 Slot liner air-gap

Each section will have a sweep of parameters and possible methods of realization taken from literature and inference.

5.3 EQUIVALENT THERMAL CONDUCTIVITY OF THE SLOT

5.3.1 *Rated Current*

The thermal conductivity of the slot is a combination of the different materials in it. The potting compound is the largest contributor to the overall thermal conductivity. A sweep will be done considering two values of potting conductivity λ, 2.5 W/m.K and 20 W/m.K. As mentioned at the beginning, three mechanical design configurations would be tested. A separate FEM simulation was run to calculate the equivalent conductivity of the combination of winding and impregnation. A goodness factor of 0.7 was considered which can be expected by using a degassing method (VPI).

5.3.1.1 *Current Design*

The current design has the aluminium channel only until the stator laminations. The potted end-windings are exposed to only air on three sides making it rather difficult for heat flux to leave this region. Under certain operating conditions, the rotating outer rotor can influence the velocity of air in the end region slightly reducing the resistance to the air. The use of a higher thermal conductivity potting with this design reduces the resistance between the copper and the slot liner. Fig. 41 shows the temperature characteristics of the hotspot with varying thermal conductivities. The initial temperatures were set to 55degC for both the fluid and the winding region. The use of a 20 W/mK potting compound reduces the temperature after 30 minutes by 4.3%. Despite reducing the thermal resistance of the slot, there are still air gaps which dominate. The magnet temperature does not vary much with the change in the potting compound despite doubling the thermal conductivity of the air-gap.

5.3.1.2 *Coolant housing extension*

The influence of the thermal conductivities was tested with the aluminium housing extended. The contact between the end region potting and the housing was considered to be continuous (no air-gaps). With the current potting compound this additional path for heat to flow from the end windings does not do more than that of the air in the absence of this extension. However advantages start to show as we increase the thermal conductivity. As much as 11.5% improvement can be seen in Fig.43 by using a higher thermal conductivity potting.

5.3.1.3 *Housing extension with additional channels*

There can be additional channels carved out of the housing on both end regions. The current model considers two extra channels of dimensions similar to that of their adjacent channels. The flow rate has to be slightly increased from 10 to 13.5 lit/min to maintain the same heat transfer coefficient in the other channels. The model predicts a greater reduction in hotspot temperatures with a high thermal conductivity compound. Temperature drops of 7.4% and 19% can be predicted by using potting compounds of 2.5 and 20 W/mK respectively.

5.3.2 *Peak Current*

The extension of the housing or addition of extra channels did not effect the behaviour of the model under very short operating times.

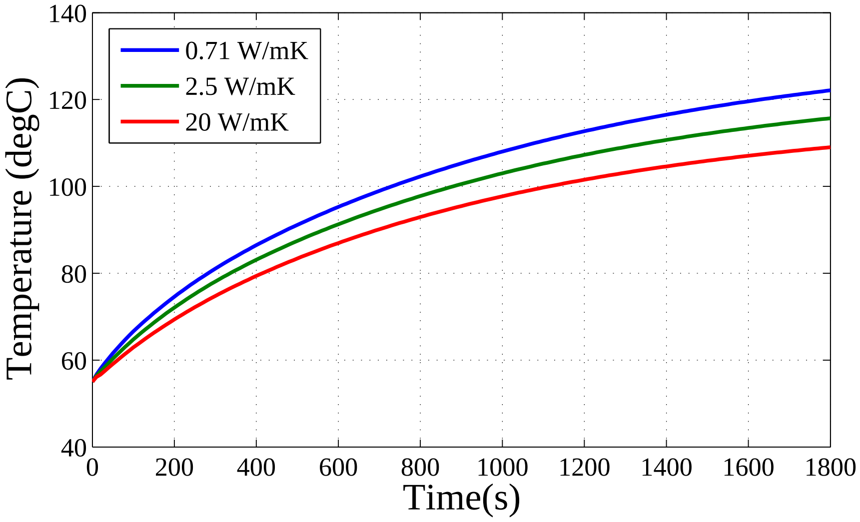

Figure 41: Variation of slot hotspot temperature with change in potting compound - Current Design

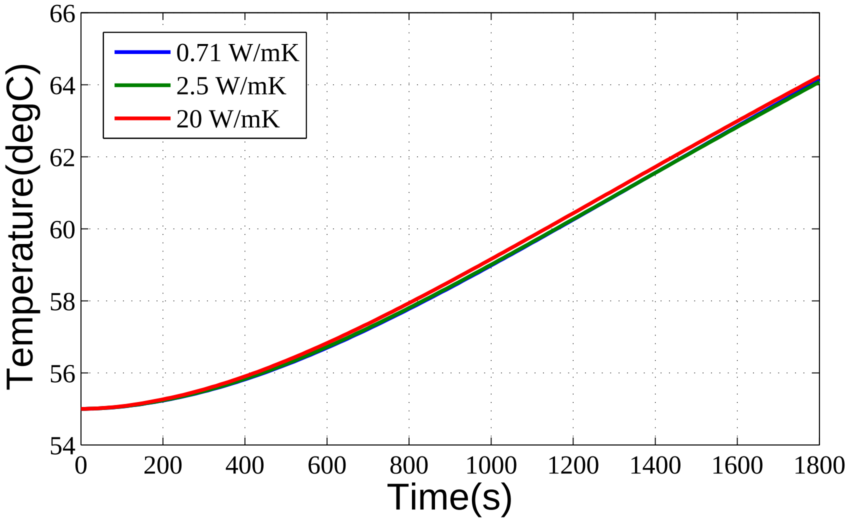

Figure 42: Variation of magnet temperature with change in potting compound - Current design

This is because the heat capacity of the potting compound is large enough to prevent any influence from outside the slot in short periods. The hotspot in the case of this test was in the centre of the slot and not on the end windings due to the large capacitance of the potting compound in the end regions. The results are similar for all three mechanical design considerations. Fig. 47 shows the influence of three thermal conductivity values on the hotspot temperature all having the same heat capacity (can be calculated from [16]). A very important factor that is more obvious now is the value of the specific heat capacity for the potting compound. For higher values of specific

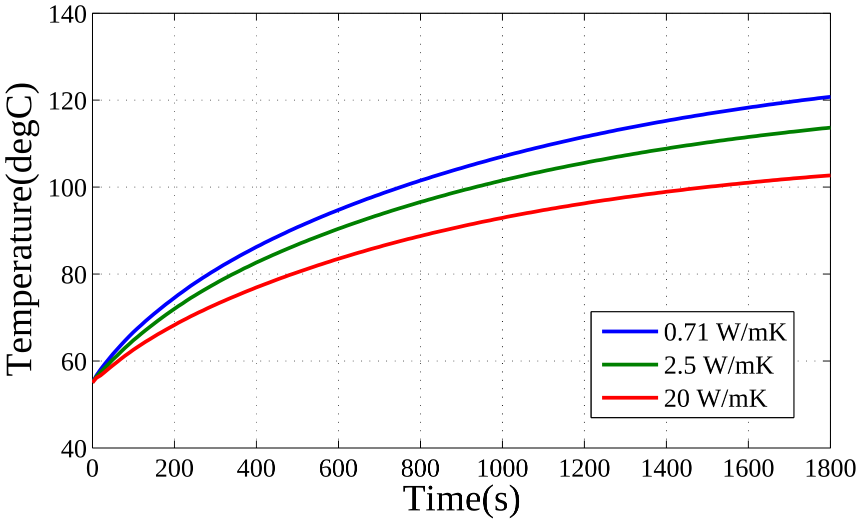

Figure 43: Variation of slot hotspot temperature with change in potting compound - Extended housing

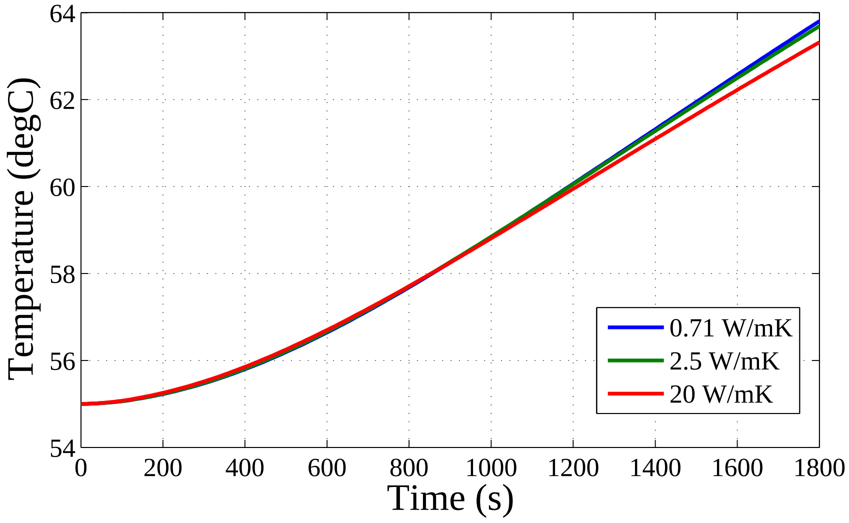

Figure 44: Variation of magnet temperature with change in potting compound - Extended housing

heat capacity, the hot spot would be lower for a short period and vice-versa.

5.3.3 *Possible methods of realization*

There has been very little research on new materials for potting applications with increased thermal conductivity. Nategh et al. performed a study to compare the effect of different impregnating compounds on the machine hotspot temperature. A silicone based thermally conductive material later found to be called **Lord's SC-320** having a ther-

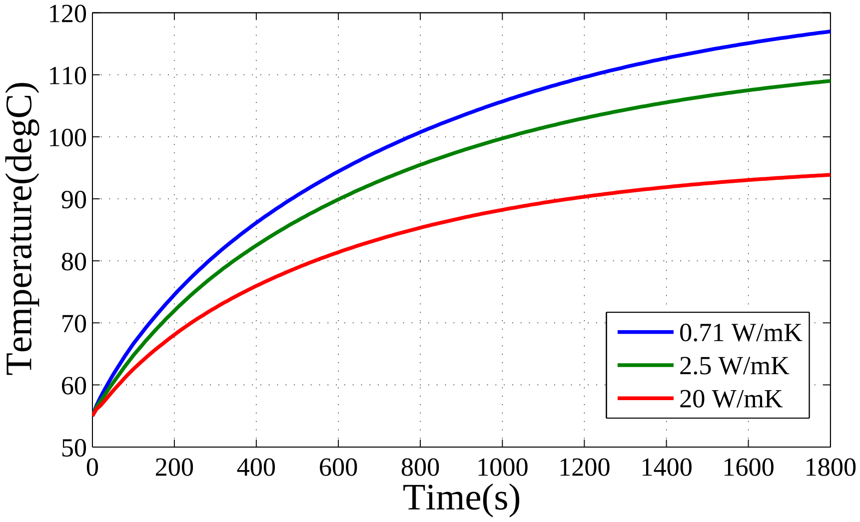

Figure 45: Variation of slot hotspot temperature with change in potting compound - Extended housing with additional channels

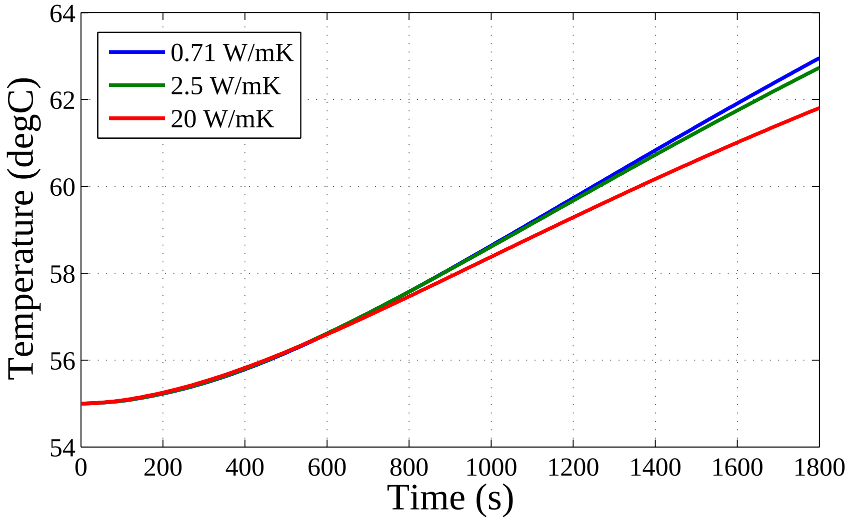

Figure 46: Variation of magnet temperature with change in potting compound - Extended housing with additional channels

mal conductivity of **3.2 W/mK** was found to have the most influence on the temperature.

Certain compounds called *fillers* in their powdered form can be added to polymers to increase the thermal conductivity. Compounds like Aluminium Oxide, Aluminium Nitride, Boron Nitride etc., are mixed into the polymer matrix in a micro or nano-particle form. The process is generally easy but requires proper de-gassing (Vacuum based) and careful selection of the filler shapes (Porous, spherical etc.). Yao et al. used **AlN** as a filler in a single-composite potting compound and reached thermal conductivities close to **40 W/mK** which is twice as high as what was tested in the model. By utilizing such materials in the machine, the temperatures can be considerably reduced allowing higher currents to be used for longer times.

Polikarpova et al. uses two potting compounds, **Ceramacast** and a high temperature **Epoxy 2315** in a 100kW radial flux PMSM. The thermal conductivities were **100 W/mK** and **58 W/mK** respectively which are again higher than the model simulations. The machine dealt with in the previous study utilizes the potting in small volumes to link the end windings and the coolant housing. This allows a smaller quantity to be used and yet reduce machine temperatures.

If we consider the machines design, a high thermally conductive ceramic material can be used between the existing potting and the suggested housing extension. This would look something like as shown in Fig. 48

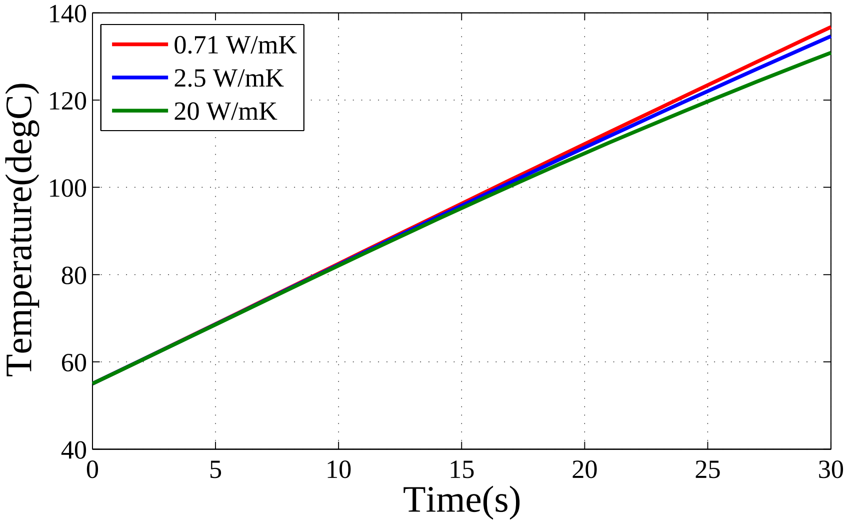

Figure 47: Variation of slot hotspot temperature with change in potting - 750A (same for all mechanical design variations)

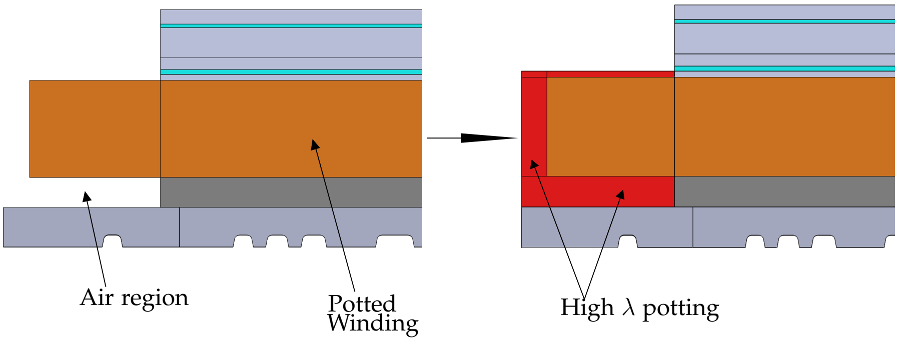

Figure 48: Before and After region-specific potting

The model was simulated in a similar manner, with only the sides of the end regions potted with a high thermally conductive material and the rest containing the standard encapsulate. The temperatures are shown in Fig. 49 where a 40 W/mK compound applied at the sides can reduce the temperature by about 14%.

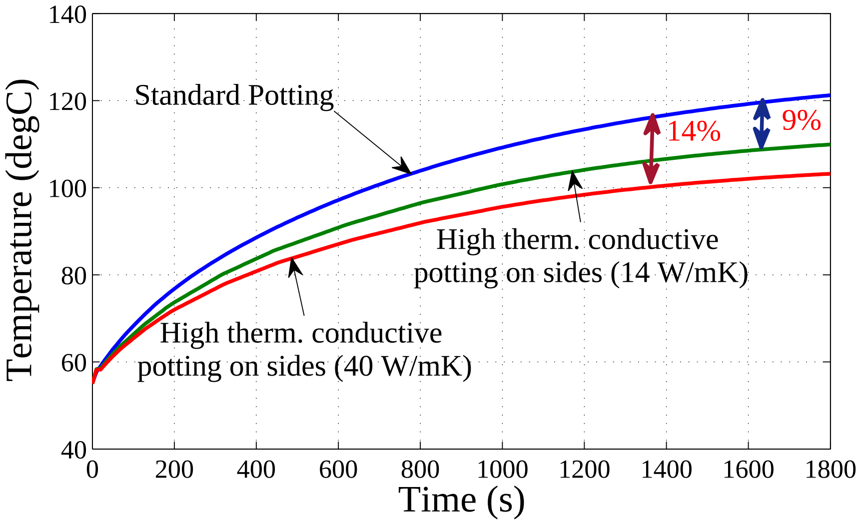

Figure 49: Using good thermal potting on the sides

The method of potting is also a very important governing factor to rate the effectiveness of using a particular compound. The *goodness factor* which was defined in earlier chapters can very easily drop the effective thermal conductivity to one half of its original value if care is not taken. Richnow et al. mentions the different techniques usually employed for winding impregnation and how the thermal performance and lifetimes vary depending on the method. Using a vacuum chamber is said to have an improved goodness factor (Nategh et al.) and a better chance that the compound will seep into the narrow air-gaps.

5.4 INFLUENCE OF SLOT-LINER AIR GAP

There is a region of air between the slot-liner and the stator laminations. There is very little literature on this topic and thus the exact value is hard to predict. The thickness of this air region also tends to change as the potting expands making it an even more difficult task to quantify this gap. The extent to which a reduction in this gap can reduce the machine temperatures can however be explored.

5.4.1 *Rated Current*

The model initially assumes a asymptotic function for this value of air-gap with the final value of 0.3mm. The sweep is performed by maintaining the shape of the function but reducing the overall values by a half and a quarter. Fig. 50 shows the hotspot temperatures for the first operating scenario. There is a possibility of reducing the temperatures by 9% by quartering the air-gap.

The simulation of the second high current scenario revealed that changes in the air-gap have very little effect on the short transient temperatures resulting in more or less the same temperature curve and hence is not shown. This is because of the thermal capacitance of the winding region which has to heat up first before the heat flux reaches the slot liner region.

5.4.2 *Peak Current*

The reduction of the equivalent air-gap of the slot liner resulted in lower hotspot temperatures. This is because of the lower thermal resistance in the direction of the the heat flux. The influence of this parameter is shown in Fig.51. A maximum reduction of 6.6% is predicted by quartering the air-gap.

5.4.3 *Possible methods of realization*

Owing to the difficulty in quantification of the air-gaps, suggesting improvements is rather uncertain. The current model assumes a certain breakup between the liner air-gap and the housing interface air-gap. This ratio may not be certain and thus the extent to which a change in these parameters will effect the hotspot temperature can be up for debate. However performing changes may not require a great deal of effort and thus can be recommended. We can eliminate this parasitic thermal resistance by studying it's cause. The slot liner is inserted into the slot well before the windings are laid or the potting is applied. There is no pressure holding the liner over the laminations and because the liner material is flexible in nature, there will be natural air pockets beneath it.

The use of an adhesive slot-liner during the early stages of design may help hold the slot liner to the laminations temporarily until the windings are potted. There are however limitations to this approach, like having to hand press the liner to the core resulting in additional

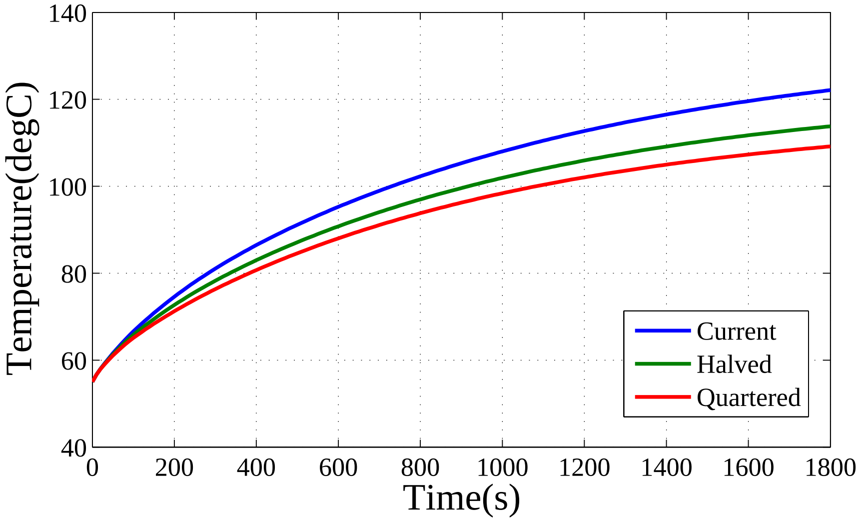

Figure 50: Variation of slot hotspot temperature with change in parasitic air-gap - Rated Current

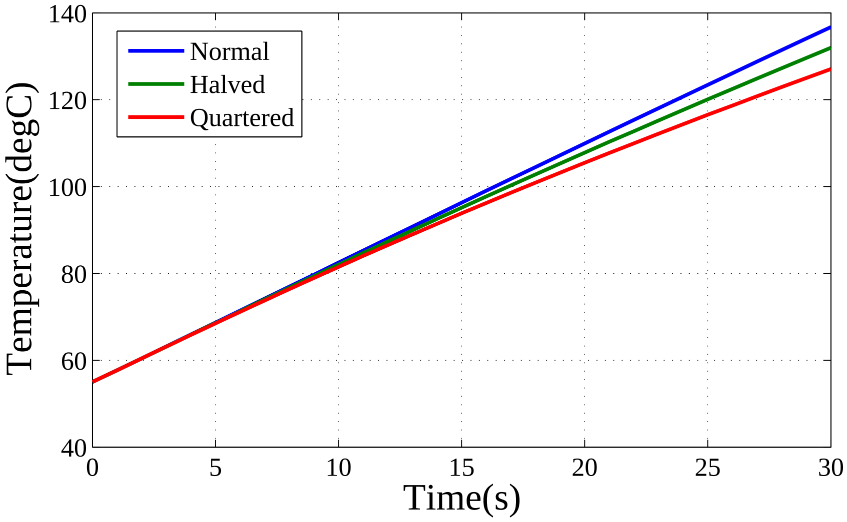

Figure 51: Variation of slot hotspot temperature with change in parasitic air-gap - 750A

time spent during manufacturing. Slot liners may also be applied automatically by a machine and in this situation, using adhesive insulation may not be an easy approach.

Another approach would be to adopt the Vacuum Pressure Impregnation method. The additional pressure may help the uncured impregnate to seep in between the liner and the core. This would however require that this region is accessible by the compound meaning that there is sufficient space for the resin to enter. The viscosity of the potting compound also influences this action i.e. a high viscosity material would require more pressure and may not penetrate into small gaps.

5.5 OTHER FACTORS

The other parameters that may contribute to the reduction in hotspot temperatures are:

5.5.1 Stator-Housing Interface

5.5.2 Location of cooling channels

5.5.3 Coolant flow rate

5.5.1 *Stator-Housing Interface*

The equivalent air-gap between the stator core and the coolant housing plays a vital role in heat transfer. The two bodies are fit with what is called an *interference or shrink fit* and irregularities may exist at the interface. In reality there is a possibility that the slot liner air-gap is much smaller, and the housing-gap is slightly larger (resulting in the same hotspot temperature).

In such a scenario, the reduction in the housing air-gap may result in a reduced hotspot temperature. This can be accomplished by slightly (minute changes cause large pressures) increasing the diameter of the inner cooling bush at room temperature. This would result in a tighter fit (higher contact pressure) which in-turn leads to a lower air-gap. This method is however restricted by one factor, the smoothness of the two surfaces. If either of the surfaces are rough, any increase in pressure might not result in a higher contact conductance. On the contrary, a smoother surface may also increase contact conductance at the same pressure.

5.5.2 *Location of cooling channels*

There are numerous possibilities that exist for the location of the cooling channels. The current design uses an aluminium housing that encloses the channels. The question will always arise,*"What if the cooling channels are placed where the heat is generated (within the slot)?"*. Though the idea may lead to a much better cooling, there are many disadvantages.

The addition of cooling channels in the slot would result in a reduced fill factor (some windings have to be replaced to make room for the channel) which in turn diminishes the current density. The fill factor problem can be slightly alleviated by using rectangular conductors which helps in compensating for the lost copper area. However rectangular windings would mostly result in an ordered arrangement of conductors within the slot and this results in higher proximity effect related losses.

From a mechanical point of view, the channels would leave one slot and enter the consecutive one in a continuous manner till the entire periphery is covered. There could also be a parallel split up of the channels each covering a fraction of the total number of slots. The first difficulty would arise in maintaining an equal flow distribution in n parallel channels. The second complexity arises from the dimensions of the channels i.e. the small slot would accommodate a channel with a small diameter and the large number of slots would result in long channels. Both these characteristics lead to a higher pressure drop (recalling eqn.25) and thus a higher pumping power requirement.

Thermal expansion in the slots could also be a problem causing cracks on the channel walls leading to leakage. Channels made of metal may also suffer from induced iron losses from adjacent conductors. If all these are solved, the design may be considered and modelled. As can be seen, there are multiple circumstances that have to be studied and hence simulation of this concept is beyond the scope of this thesis.

5.5.3 *Flow rate*

The flow rate of the coolant decides the heat transfer coefficient on the channel wall and thus a higher flow rate would be expected to result in a lower hotspot temperature. This assumption under most circumstances would be true, but if there are much higher thermal resistances in the path of the heat flow, a further reduction in the lowest thermal resistance (Heat transfer coefficient) does not cause much of a change. This is the situation that occurs in the studied machine. Fig. 52 shows the hotspot temperatures with 10lit/min and 25lit/min flow rates. CFD calculated the heat transfer coefficients at 25lit/min to be roughly about two times that of 10lit/min. The model predicts a temperature difference of hardly 4 °C between the two. It should be noted that the resistance to flow offered by the pipe varies as the square of mass flow, thus a $2\frac{1}{2}$ times increase in flow requires almost 6 times the pumping power.

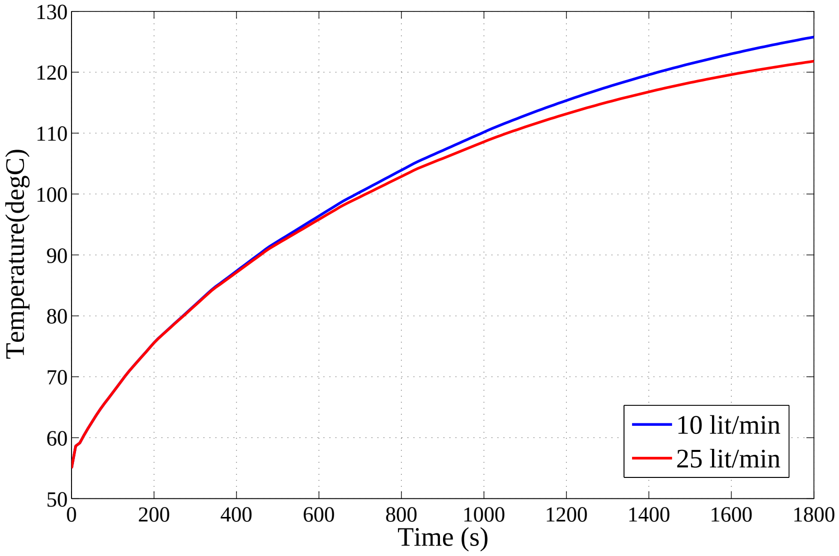

Figure 52: The influence of flow rate on the hotspot temperature

5.6 CONCLUSIONS

The extent to which changes in the materials or design would effect the hotspot temperature were initially unknown. With the help of a numerical model, such effects were quantified. With the right combination of design and material changes, temperature drops of up to 29% were seen. The model was also very helpful at predicting temperatures at currents which could not yet be realized practically. The end winding regions get the hottest during operation and the extraction of heat directly from these regions by the coolant housing ensures that large thermal barriers can be bypassed.

6

CONCLUSIONS

This chapter concludes all the work done as part of the thesis and discusses the inferences that were drawn. There are also suggestions for carrying out the work in the future to further develop this study.

6.1 SUMMARY

The aim of this thesis was to develop a model that could predict the hotspot temperatures within a surface mounted outer-rotor PMSM and to use this model to predict the extent to which thermal improvements could be made. The thermal model was chosen to be of numerical type particularly using the Finite Element Method. During the design stage, many unknown parameters had to be resolved and thus literature was explored to uncover approximate values for these parameters. A FEM simulation was performed to calculate the slot equivalent thermal conductivity to incorporate the influence of the copper, the winding insulation and the potting compound. The rough interfaces between certain materials were represented using an equivalent air-gap and their values were found to vary as a function of temperature.

A brief introduction to fluid dynamics was given followed by a Computational Fluid Dynamics based simulation in ANSYS to calculate the heat transfer coefficient between the coolant and the housing. An additional study was made to characterize the flow of liquid in a curved pipe and comparisons were made between simulation and literature. The various values calculated in the earlier stages were applied to a COMSOL model in order to estimate the machine temperatures. Experiments were performed under different operating conditions and results were compared with the FEM model. Temperatures were found to adhere to within 5% of the experimental results.

Suggestions for improvement of the thermal performance of the machine were studied. The influential parameters were isolated and design changes were simulated. The thermal conductivity of the potting compound was a considerable barrier to heat flow and various thermal conductivities were simulated to seek reductions in temperature. Studies where higher thermal conductivity potting compounds were utilized were beneficial in proposing material changes. The air-gap between the slot-liner and the stator also hindered the heat flow and thus suggestions were offered that could help reduce this. The housing was extended till the end winding regions and additional channels were modelled. It was found that this design variation had a very little effect with the existing potting compound. The following conclusions were drawn:

The slot hotspot temperature can be reduced by approximately:-

1. 10% by using a high thermal conductivity compound.
2. 16% by further extending the coolant housing towards the end region.
3. 23% by further adding extra cooling channels to the coolant housing.
4. 10% by quartering the effective air-gap between slot liner and stator core.

By using materials like Ceramacast and Lord's SC-320 there are possibilities of achieving the mentioned temperature improvements. Filler compounds can also be embedded into the matrix to help serve this purpose. It was also seen that additionally only potting the region beneath the end winding with a high λ material had a considerable effect on the hotspot temperature. Vacuum impregnation techniques help reduce the air-bubbles within the potting and the slot-liner parasitic air-gap. An extension of the housing is also proposed as a method to bypass the high thermal resistance barriers.

6.2 PROPOSALS FOR FUTURE WORK

The heat transfer coefficient in the end region is rather complex to assess and thus using experimental results from literature is the most sought after solution. If proper computational power is present, a CFD simulation of this region can be done which offers more insight into how the current design influences the heat transfer coefficient and how improvements could be made to enhance this value. The same applies to the cooling channel region i.e. if sufficient resources are made available, the entire region can be simulated which might help observe the behaviour of the fluid in the distribution region.

The coolant housing air-gap was found to vary as a function of temperature on account of thermal expansion. This effect could not be however quantified due to limitations in experimental apparatus. By isolating this region practically and performing a heat transfer analysis, the temperature drop and hence the thermal resistance can be estimated. From this value the slot-liner air-gap can approximately be quantified. After an initial estimation, a structural FEM simulation can be run to calculate the variation of the contact conductance with temperature.

The presence of more sensors at carefully chosen locations within the machine can offer more data for comparison. The search for new thermally enhanced potting materials should be continued as part of future studies and laboratory made composites can be tested reducing dependence on literature. In chapter 5 new materials were proposed that need to be verified practically by real potting to take into account the influence of the method. A cross section of the cured compound should also be observed so as to visualize the air bubbles in the interior.

****

BIBLIOGRAPHY

[1] Thomas Finken, Matthias Felden, and Kay Hameyer. Comparison and design of different electrical machine types regarding their applicability in hybrid electrical vehicles. *Proceedings of the 2008 International Conference on Electrical Machines, ICEM'08*, pages 1–5, 2008. doi: 10.1109/ICELMACH.2008.4800044.

[2] Florian Demmelmayr, Markus Troyer, and Manfred Schroedl. Advantages of PM-machines compared to induction machines in terms of efficiency and sensorless control in traction applications. *IECON Proceedings (Industrial Electronics Conference)*, pages 2762–2768, 2011. ISSN 1553-572X. doi: 10.1109/IECON.2011.6119749.

[3] Gunter Freitag, Markus Klopzig, Klaus Schleicher, Markus Wilke, and Marco Schramm. High-performance and highly efficient electric wheel hub drive in automotive design. In *2013 3rd International Electric Drives Production Conference, EDPC 2013 - Proceedings*, 2013. ISBN 978-1-4799-1105-9. doi: 10.1109/EDPC.2013.6689736.

[4] Kersten Reis and Andreas Binder. Development of a permanent magnet outer rotor direct drive for use in wheel-hub drives. In *Electrical Machines (ICEM), 2014 International Conference on*, pages 2424–2430, 2014. ISBN 9781479943890.

[5] D. J. Van Schalkwyk and M. J. Kamper. Effect of hub motor mass on stability and comfort of electric vehicles. *2006 IEEE Vehicle Power and Propulsion Conference, VPPC 2006*, 2006. doi: 10.1109/VPPC.2006.364297.

[6] Y.K. Chin and D.a. Staton. Transient thermal analysis using both lumped-circuit approach and finite element method of a permanent magnet traction motor. *2004 IEEE Africon. 7th Africon Conference in Africa (IEEE Cat. No.04CH37590)*, 2, 2004. doi: 10.1109/AFRICON.2004.1406847.

[7] Janne Nerg, Marko Rilla, and Juha Pyrhönen. Thermal analysis of radial-flux electrical machines with a high power density. *IEEE Transactions on Industrial Electronics*, 55(10):3543–3554, 2008. ISSN 02780046. doi: 10.1109/TIE.2008.927403.

[8] David G. Dorrell. Combined thermal and electromagnetic analysis of permanent-magnet and induction machines to aid calculation. *IEEE Transactions on Industrial Electronics*, 55(10):3566–3574, 2008. ISSN 02780046. doi: 10.1109/TIE.2008.925311.

[9] Dave Staton, Aldo Boglietti, and Andrea Cavagnino. Solving the more difficult aspects of electric motor thermal analysis in small and medium size industrial induction motors. *IEEE Transactions on Energy Conversion*, 20(3):620–628, 2005. ISSN 08858969. doi: 10.1109/TEC.2005.847979. URL http://ieeexplore.ieee.org/xpls/abs_all.jsp?arnumber=1495534.

[10] Aldo Boglietti, Andrea Cavagnino, and Dave Staton. Determination of critical parameters in electrical machine thermal models. *IEEE Transactions on Industry Applications*, 44(4):1150–1159, 2008. ISSN 00939994. doi: 10.1109/TIA.2008.926233.

[11] Fabrizio Marignetti, Vincenzo Delli Colli, and Yuri Coia. Design of axial flux PM synchronous machines through 3-D coupled electromagnetic thermal and fluid-dynamical finite-element analysis. *IEEE Transactions on Industrial Electronics*, 55(10):3591–3601, 2008. ISSN 02780046. doi: 10.1109/TIE.2008.2005017.

[12] Wenying Jiang and T. M. Jahns. Coupled electromagnetic-thermal analysis of electric machines including transient operation based on finite element techniques. *2013 IEEE Energy Conversion Congress and Exposition*, pages 4356–4363, 2013. doi: 10.1109/ECCE.2013.6647283. URL http://ieeexplore.ieee.org/lpdocs/epic03/wrapper.htm?arnumber=6647283.

[13] Shafigh Nategh, Zhe Huang, Andreas Krings, Oskar Wallmark, and Mats Leksell. Thermal modeling of directly cooled electric machines using lumped parameter and limited cfd analysis. *IEEE Transactions on Energy Conversion*, 28(4):979–990, 2013. ISSN 08858969. doi: 10.1109/TEC.2013.2283089.

[14] Michael Galea, Chris Gerada, Tsarafidy Raminosoa, and Patrick Wheeler. A thermal improvement technique for the phase windings of electrical machines. *IEEE Transactions on Industry Applications*, 48(1):79–87, 2012. ISSN 00939994. doi: 10.1109/TIA.2011.2175470.

[15] Gilles Guedia Guemo, Student Member, Patrice Chantrenne, and Julien Jac. Parameter Identification of a Lumped Parameter Thermal Model for a Permanent Magnet Synchronous Machine. In *Electric Machines & Drives Conference (IEMDC), 2013 IEEE International*, pages 1316–1320, 2013. ISBN 9781467349741.

[16] Nick Simpson, Rafal Wrobel, and Phil H. Mellor. Estimation of equivalent thermal parameters of impregnated electrical windings. *IEEE Transactions on Industry Applications*, 49(6):2505–2515, 2013. ISSN 00939994. doi: 10.1109/TIA.2013.2263271. URL http://ieeexplore.ieee.org/xpls/abs_all.jsp?arnumber=6516549.

[17] Shafigh Nategh, Andreas Krings, Oskar Wallmark, and Mats Leksell. Evaluation of impregnation materials for thermal management of liquid-cooled electric machines. *IEEE Transactions on Industrial Electronics*, 61(11):5956–5965, 2014. ISSN 02780046. doi: 10.1109/TIE.2014.2308151. URL http://ieeexplore.ieee.org/xpls/abs_all.jsp?arnumber=6748978.

[18] Louis J. Salerno and Peter Kittel. *Thermal Contact Conductance*. 1997. ISBN 9783319012759. doi: 10.1007/978-3-319-01276-6.

[19] Devdatta P. Kulkarni, Gabriel Rupertus, and Edward Chen. Experimental investigation of contact resistance for water cooled jacket for electric motors and generators. *IEEE Transactions on Energy Conversion*, 27(1):204–210, 2012. ISSN 08858969. doi: 10.1109/TEC.2011.2177465. URL http://ieeexplore.ieee.org/xpls/abs_all.jsp?arnumber=6107570.

[20] R Camilleri, D a Howey, and M D Mcculloch. Experimental investigation of the thermal contact resistance in shrink fit assemblies with relevance to electrical machines. *IET Power Electronics Machines and Drives Conference (PEMD)*, 2014.

[21] Gunnar Kylander. *Thermal modelling of small cage induction motors*. Phd disssertation, Chalmers University of Technology, Sweden, 1995. URL http://webfiles.portal.chalmers.se/et/PhD/KylanderGunnarPhD.pdf.

[22] Juha Pyrhönen, Tapani Jokinen, and Valéria Hrabovcová. *Design of Rotating Electrical Machines*. 2008. ISBN 9780470695166. doi: 10.1002/9780470740095.

[23] Jiyuan Tu, Guan Yeoh, and Chaoqun Liu. *Computational Fluid Dynamics: A Practical Approach*. Elsevier, 2013. ISBN 978-0-7506-8563-4.

[24] Frank P Incropera, David P DeWitt, Theodore L Bergman, and Adrienne Lavine. Fundamentals of heat and mass transfer, 2007.

[25] Prn Childs and Ca Long. A review of forced convective heat transfer in stationary and rotating annuli. *Journal of Mechanical Engineering Science*, 210, 1996. URL http://pic.sagepub.com/content/210/2/123.short.

[26] M. Fénot, Y. Bertin, E. Dorignac, and G. Lalizel. A review of heat transfer between concentric rotating cylinders with or without axial flow. *International Journal of Thermal Sciences*, 50(7): 1138–1155, July 2011. ISSN 12900729. doi: 10.1016/j.ijthermalsci.2011.02.013. URL http://linkinghub.elsevier.com/retrieve/pii/S1290072911000548.

[27] David a. Howey, P. R N Childs, and Andrew S. Holmes. Air-gap convection in rotating electrical machines. *IEEE Transactions on Industrial Electronics*, 59(3):1367–1375, 2012. ISSN 02780046. doi: 10.1109/TIE.2010.2100337.

[28] Aldo Boglietti, Andrea Cavagnino, David a. Staton, Mircea Popescu, Calum Cossar, and Malcolm I. McGilp. End space heat transfer coefficient determination for different induction motor enclosure types. *IEEE Transactions on Industry Applications*, 45(3): 929–937, 2009. ISSN 00939994. doi: 10.1109/TIA.2009.2018967.

[29] BariÅ Özerdem. Measurement of convective heat transfer coefficient for a horizontal cylinder rotating in quiescent air. *International Communications in Heat and Mass Transfer*, 27(3):389–395, 2000. ISSN 07351933. doi: 10.1016/S0735-1933(00)00119-6.

[30] Ivan Di Piazza and Michele Ciofalo. Transition to turbulence in toroidal pipes. *Journal of Fluid Mechanics*, 687:72–117, October 2011. ISSN 0022-1120. doi: 10.1017/jfm.2011.321. URL http://www.journals.cambridge.org/abstract_S0022112011003211.

[31] C. M. White. Streamline Flow through Curved Pipes. *Proceedings of the Royal Society A: Mathematical, Physical and Engineering Sciences*, 123(792):645–663, 1929. ISSN 1364-5021. doi: 10.1098/rspa.1929.0089. URL http://rspa.royalsocietypublishing.org/content/royprsa/123/792/645.full.pdf.

[32] R a Seban, E F Mclaughlint, and Lawrence Radiation Labora. Heat Transfer in Tube Coils With Laminar Flow and. *Int. J. Heat Mass Transfer*, 6:387–395, 1963.

[33] Yasuo Mori and Wataru Nakayama. Study on Forced Convective Heat Transfer in Curved Pipes : 1st Report, Laminar Region. *Transactions of the Japan Society of Mechanical Engineers*, 30(216): 977–988, 1964. ISSN 0029-0270. doi: 10.1299/kikai1938.30.977.

[34] G. J. Hwang and Chung-Hsing Chao. Forced Laminar Convection in a Curved Isothermal Square Duct. *Journal of Heat Transfer*, 113(1):48, 1991. ISSN 00221481. doi: 10.1115/1.2910550. URL http://heattransfer.asmedigitalcollection.asme.org/article.aspx?articleid=1440625.

[35] Paisarn Naphon and Somchai Wongwises. A review of flow and heat transfer characteristics in curved tubes. *Renewable and Sustainable Energy Reviews*, 10(5):463–490, October 2006. ISSN 13640321. doi: 10.1016/j.rser.2004.09.014. URL http://linkinghub.elsevier.com/retrieve/pii/S1364032104001339.

[36] Yi Yao, Lingyun Gu, Tao Fan, Wei Sun, and Jian Luo. Evaluation of heat transfer characteristic of Aluminum Nitride (AlN) pot-

ting compound for the end windings of permanent magnet synchronous machines. *2011 International Conference on Electrical and Control Engineering, ICECE 2011 - Proceedings*, pages 4498–4501, 2011. doi: 10.1109/ICECENG.2011.6057645.

[37] M Polikarpova, P M Lindh, J A Tapia, and J J Pyrhönen. Application of Potting Material for a 100 kW Radial Flux PMSM. In *Electrical Machines (ICEM), 2014 International Conference on*, pages 1–6, 2014. ISBN 9781479943890.

[38] J Richnow, P Stenzel, A Renner, D Gerling, C Endisch, Audi Ag, and D Ingolstadt. Influence of Different Impregnation Methods and Resins on Thermal Behavior and Lifetime of Electrical Stators. In *Electric Drives Production Conference (EDPC), 2014 4th International*, 2014. ISBN 9781479950096.